# Diversity and single-cell activity of endolithic microbes in sediment-hosted carbonate nodules within and below the sulfate-methane transition zone

Sergio A. Parra[a*]#, Magdalena J. Mayr[a,b], James Mullahoo[a], Laura K. Quinn[c&], Rebecca L. Wipfler[a], Victoria J. Orphan[a,b]#

[a]Division of Geological and Planetary Sciences, California Institute of Technology, Pasadena, California, USA

[b]Division of Biology and Biological Engineering, California Institute of Technology, Pasadena, California, USA

[c]Division of Chemistry and Chemical Engineering, California Institute of Technology, Pasadena, California, USA

Running Head: **Endolithic microbes in carbonate nodules**

[*]Present Address: Sergio A. Parra, Boston Consulting Group, Los Angeles, CA, USA.

#Address correspondence to Sergio A. Parra, serg.a.parra@gmail.com; Victoria J. Orphan, vorphan@caltech.edu.

[&]Present Address: Laura K. Quinn, Saint-Gobain Ceramics & Plastics, Inc., Northborough, MA, USA

## Abstract

Authigenic carbonate concretions ('nodules') precipitate in marine seep sediments as a result of anaerobic oxidation of methane (AOM). These rocks host active endolithic microbial communities and persist as important methane sinks. Still, how these communities and their activity differ from those in adjacent seep sediments, particularly as a function of proximity to the sulfate-methane transition zone (SMTZ), remains understudied. Here, we sampled sediments and nodules within and below the SMTZ (0-57 cm deep) at four active deep-sea seep areas in Santa Monica Basin, CA. Measurements of high nodule porosities (43-51%) coupled to strong similarities between sediment and nodule 16S rRNA-based community profiles, including below the SMTZ, suggest continued perfusion and exchange between buried nodules and surrounding sediment. Shared, depth-dependent transitions in methanotrophic taxa (ANME-1, ANME-2, ANME-3) and methanogenic taxa (*Methanofastidiosales*) below the SMTZ were also consistent with trends in porewater methane and sulfate concentrations, porewater DIC, and nodule $\delta^{13}C$ values — underscoring the impact of different geochemical conditions on community structure and suggestive of under-characterized physiological plasticity in ANME-1. Laboratory-based BONCAT incubations of nodules within the SMTZ over ~14-weeks revealed active sulfide production and translationally active endolithic microorganisms. However, cells from parallel nodule incubations recovered below the SMTZ showed weak-to-negligible BONCAT-based activity despite similar cell abundances — suggestive of low activity on shorter timescales or dormancy. Together, these data challenge the interpretation of passively recorded microbiological signatures in seep sediment-hosted carbonate nodules and expand our understanding of how these endolithic communities may be actively shaped by past and present conditions.

## Importance

This study advances earlier investigations of microbial communities in buried seep carbonate nodules by integrating microbiological profiles of nodules and sediments, sediment geochemistry, single-cell activity measurements, and nodule mineral, geochemical, and physical characteristics within and below the sulfate-methane transition zone in deep-sea methane seeps. This approach allows us to view how nodule-hosted, endolithic microbial communities change relative to their surrounding sediments across multiple geochemical contexts and better understand how formation history and environmental conditions might affect community identity and metabolic function. Results indicate that the seep nodule and surrounding sediment communities are closely linked across diverse geochemical conditions. This connectivity between sediments and carbonate nodules is distinct from that observed in exhumed seep carbonates, with implications regarding how microbial community composition within these nodules are interpreted, suggesting that instead of a passive recorder of the communities at the time of formation, these nodules appear to retain diverse, metabolically viable communities.

## Introduction

Authigenic carbonates at marine methane seeps form as the result of microbially-mediated anaerobic oxidation of methane (AOM) in sediments, which draws down a substantial amount of the subsurface methane produced at these seeps (1, 2). Because these deposits persist over geologic timescales, these carbonates have been interpreted as a record of past AOM activity in ancient marine environments (3–7). However, several lab-based measurements of elevated methane oxidation rates in recovered seep carbonates demonstrate that these rocks continue to

host viable microorganisms and AOM activity, representing a persistent methane sink whose activity and ecology remains under-studied compared to seep sediments (8–11).

In particular, vuggy carbonate concretions, or 'nodules' observed in seep sediments (12–15) have not been investigated as thoroughly as denser, seafloor-exposed seep carbonates — whose metabolically diverse, endolithic communities have been observed to differ significantly from sediments and sediment-hosted nodules collected from the same sites, e.g., (16). As such, seep nodules represent a unique opportunity to study seep carbonate microbial community structure and activity in comparison to their host sediments in geochemical context.

For example, AOM in marine sediments primarily occurs within a distinct redox regime known as the sulfate-methane transition zone (SMTZ), where syntrophic activity between anaerobic, methanotrophic (ANME) archaea and sulfate-reducing bacteria (SRB) act to consume porewater methane and sulfate (17–20). This zone of AOM activity varies in depth and thickness largely controlled by methane flux, e.g., (21), transitioning from methane-poor, sulfate-rich overlying sediment horizons to deeper sulfate-poor, methane-rich sediments. The impact of relative proximity to the SMTZ on the endolithic community structure and activity within sediment-hosted carbonate nodules remains poorly characterized, with limited sampling from existing studies focusing exclusively within this zone (14–16, 22). In sediments, this geochemical stratification often results in regimes of distinct ANME/SRB lineages indicative of niche differentiation (22–29), where the observed persistence of certain ANME clades in sulfate-depleted seep sediments remains an area of active investigation (30–32). As such, the SMTZ represents a useful comparative framework in which to study the similarities and differences with co-occurring carbonate nodules across this globally important geochemical transition zone.

Previous work examining nodules recovered from seep sediments reported high similarities in the 16S rRNA diversity and community structure with host sediments (14–16). However, the extent to which these DNA-based community profiles represent extant, metabolically viable communities actively exchanged with host sediment or preserved, ancient sediment communities remains unclear (14, 15), with implications how different traces of AOM are ultimately interpreted and/or preserved in sediment-hosted nodules.

In this study, we expanded the characterization of sediment-hosted authigenic carbonate nodules from four methane seep areas at Santa Monica Mounds 800 and 863 within the Santa Monica Basin (33). Specifically, we integrated the biological and porewater geochemical profiles of 1 m long, ROV-deployed sediment cores within active deep-sea seeps with the structural and microbiological profiles of seep carbonate nodules, effectively capturing changes in both sediment and associated nodules within and well below the SMTZ. Laboratory microcosm experiments were also used to characterize differences in bulk respiration and cellular anabolic activity by the endolithic community across this transition zone using geochemical assays and single cell bioorthogonal non-canonical amino acid tagging (BONCAT) incubations. This combined approach allows us to probe the historical and current capacity of seep carbonate nodules as hosts for continued AOM activity in geochemical context, compared to their surrounding sediments.

## Results

### Sediment and nodule sampling within Santa Monica Basin methane seeps

Nodules and sediment push cores in this study were collected in May 2021 during the WF05-21 Southern California oceanographic expedition on the *R/V Western Flyer* using the *ROV Doc*

*Ricketts*, both owned and operated by the Monterey Bay Aquarium Research Institute (MBARI). 93 samples (7 cores, 82 sediment horizons, 11 nodule horizons) were recovered in total from two active methane seep sites within the Santa Monica Basin: Santa Monica Mound Site 800 (SMM 800: 33.799438N /118.64672E; 805m depth; also known as the NE mound) and Santa Monica Mound Site 863 (SMM 863: 33.7888N /118.6683W; 863 m; also known as the SW mound); (33, 34). At these sites, we investigated 4 distinct seep areas: SMM 800-I, SMM 800-II, SMM 800-III, and SMM 863 (Fig. 1). Within each seep area, 1-2 sediment cores were collected, including 3, 1.22 m long cores (LC) and 4, standard, 30 cm long push cores (PC), with quasi-duplicate ('paired') cores taken in close spatial proximity (~30-50 cm apart) to capture comparable environments, where possible. One sediment core (PC64, SMM 800-II) was collected during a previous cruise and sampled from the same microbial mat within 5 m from the 2021 sampling location (Supplemental Material).

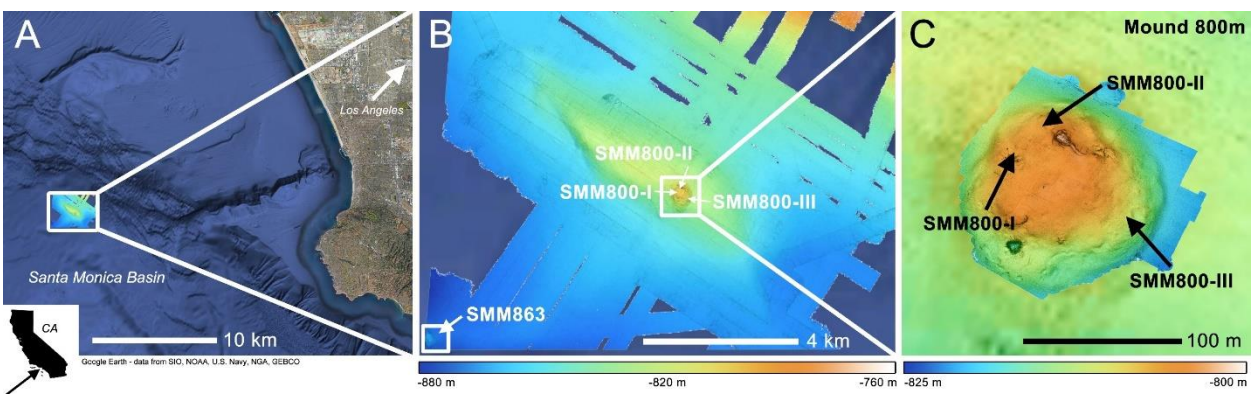


**Fig. 1** – A) General location of the Santa Monica Basin seep sites (NE Mound, 800m, and SW mound, 863m) sampled for this study; B) Multi-beam bathymetry map of the sampling seep areas at SMM 800 and SMM 863; C) higher-resolution bathymetry map of the seep areas sampled at SMM 800: SMM 800-I, SMM 800-II, and SMM 800-III. Bathymetry colors in B) and C) correspond to mapped depth. Bathymetry maps were collected by MBARI in 2018.

**Morphological diversity in seep sediment-hosted nodules**

Across both short and long sediment push cores from all four seep areas, we observed distinct depth intervals of hardened, grey-brown calcitic material ranging in size from <cm rubble to >cm

concretions, or nodules. Representative nodules from the four seep areas are shown in Fig. 2, with a complete list of the nodule-bearing sediment horizons included in this study summarized in Table S1. We observed strong morphological differences between the nodules recovered from cores at SMM 800 and SMM 863. Nodules from SMM 800 (Fig. 2A-C) were rougher, more irregularly shaped, and featured a greater number of mm to cm-sized voids. These nodules were also less friable, with lobate, grey-brown, coarse-grained growths often covering black, thin bivalve shell fragments. These features were consistent between the three seep areas sampled at SMM 800, as well as down core (7 nodule-bearing horizons total). In contrast, nodules from SMM 863 (Fig. 2D) were less irregularly shaped, with a less porous, finer grained, brown-colored material that resembled packed sediment hosting smaller lithics within. This morphology was also consistently observed between cores and across the five nodule-bearing horizons sampled at SMM 863.

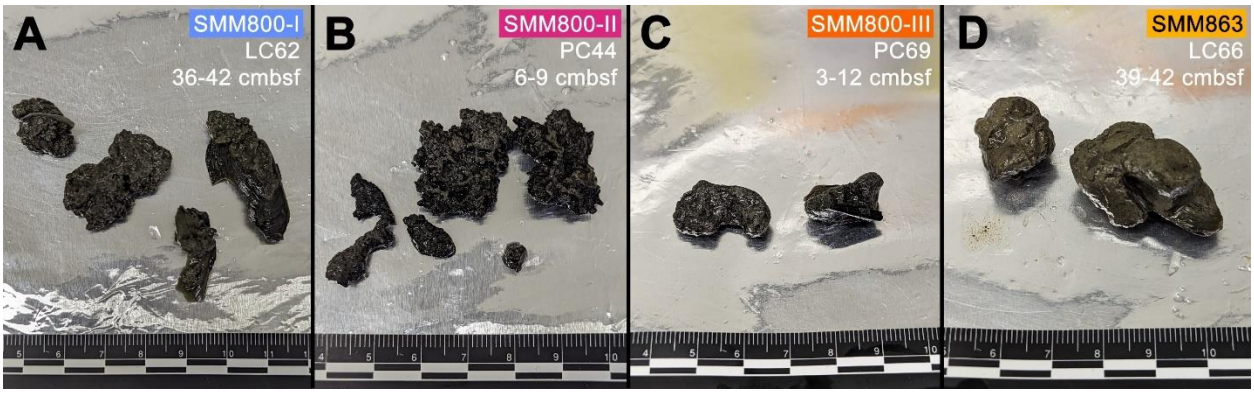


**Fig. 2** – Characteristic nodules recovered from each of the four seep areas in this study; Nodule morphology is remarkably consistent with depth (expressed as centimeters below seafloor, cmbsf); ruler markings are in cm; A) Nodules recovered from LC62's 36-42-cmbsf horizons at SMM 800-I; B) Nodules from PC44's 6-9-cmbsf horizon at SMM 800-II; C) Nodules recovered from PC69 (3-12-cmbsf) at SMM 800-III; D) Nodules recovered from the 39-42-cmbsf horizon of LC66 at SMM 863.

**Nodule porosity differences and pore size distributions**

Open porosity is defined as the volume of connected pores relative to the volume of bulk solid, effectively representing the pore space that can freely exchange with the surrounding sediment

environment. Water intrusion analyses of a subset of nodules (Table 1) revealed that the open porosities of two nodules sampled from SMM 800 (800-I, 800-II) were substantially higher than that of the nodule from SMM 863.

**Table 1**
Water intrusion-derived open porosities for select nodules

| Seep Area | SMM 800-I | SMM 800-II | SMM 863 |
|---|---|---|---|
| **Core ID** | LC62 | PC44 | LC66 |
| **Core Horizon (cmbsf)** | 36-42 | 9-12 | 39-42 |
| **Open Porosity (%)** | 51.36±0.84 | 49.52±1.33 | 43.03±0.78 |

Hg-porosimetry enabled the measurement of pore size distributions between 6 and 350 μm, revealing several pore-size regimes within a SMM 863 nodule collected at depth (39-42 cmbsf), including peaks corresponding to 11, 30, and 300 μm, and a slightly higher proportion of pores with sizes >100 μm (Fig. 3). A similarly deep-sourced nodule from SMM 800-I had fewer, although more evenly distributed pore sizes in the observed range. We also saw a smaller peak of pore diameters at 90 μm and fewer pore diameters above 100 μm compared to the nodule from SMM 863. A shallower nodule from SMM 800-II (9-12 cmbsf) also had a relatively low, but even pore-size distribution below 100 μm, in addition to the occurrence of pore sizes between 100 and 250 μm, with minor peaks at 300 and 350 μm.

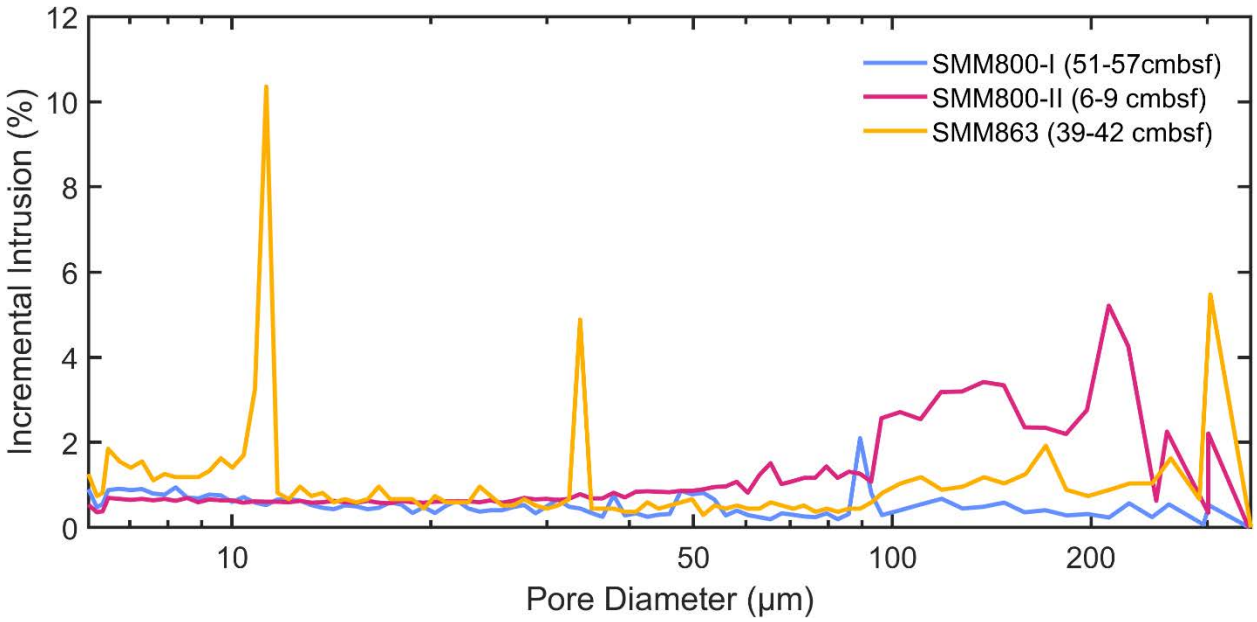


**Fig. 3** – Hg-porosimetry curves detailing pore diameter versus incremental intrusion for three nodules sampled from SMM 800-I, SMM 800-II, and SMM 863. Pore sizes observable with porosimetry range from 6- to 350-μm. The three nodules shed information on the three distinct nodule-featuring regions identified in this data set: 1) SMM 800 deep sediment (LC62), 2) SMM 800 shallow sediment (PC44), and 3) SMM 863 deep sediment (LC66)

**Aragonite dominates nodule carbonate mineralogy, with increased Mg-calcite fractions in deeper nodules**

Bulk powder XRD-derived mineralogies showed SMM 800 nodules were largely composed of aragonite (>78.2%), with minor contributions from Mg-calcite, calcite, and dolomite (Table 2). Conversely, nodules from SMM 863 were more aragonite-poor (<43.1%) and featured greater contributions from Mg-calcite (45.1%, 65.1%) than the nodules from SMM 800. Collectively, however, we did observe a greater proportion of Mg-calcite in the nodules sourced from deeper sediment horizons.

**Table 2**

Key mineral phases for select nodules, as determined by XRD

| Seep Area | Core ID | Depth (cmbsf) | Aragonite | Mg-Calcite[a] | Calcite | Dolomite | Quartz |
|---|---|---|---|---|---|---|---|
| **SMM 800-I** | LC62 | 24-27<br>48-51 | 85.2%<br>78.2% | 4.5%<br>11.3% | 0.6%<br>3.8% | 3.3%<br>0.03% | 6.4%<br>6.7% |
| **SMM 800-II** | PC44 | 9-12 | 90.2% | 2.1% | 2% | 1.6% | 3.3% |
| **SMM 800-III** | PC69 | 3-12 | 97% | 0.1% | 1.3% | 0.8% | 0.9% |
| **SMM 863** | LC74 | 33-39 | 43.1% | 45.1% | 0.5% | 4.8% | 0.5% |

| | | | | | | | |
|---|---|---|---|---|---|---|---|
| | LC66 | 39-42 | 26.1% | 65.1% | 7.1% | 1.6% | 0.03% |

*a: Mg-Calcite corresponds to* $(Ca_{0.9}Mg_{0.1})O_3$*, as measured by* (35)

**Geochemical localization of the SMTZ and $\delta^{13}C$ trends in porewater DIC and nodules**

To characterize the geochemical environments at SMM 800 and SMM 863, we focused on the vertical trends of three characteristic porewater species that inform the sulfate-methane transition zone (SMTZ): methane ($CH_4$), sulfate ($SO_4^{2-}$), and sulfide ($H_2S$), shown in Fig. 4. At SMM 800-I (LC62) collected within a sulfur-oxidizing microbial mat (Fig. S1), porewater extracts revealed high AOM activity, with a near-complete drop in sulfate concentration by 6-9 cmbsf, which remained low down core (Fig. 4A). This drop was matched by a concurrent rise in porewater sulfide and methane, although we observed more dynamic behavior in the sulfide and methane concentrations with depth, including a notable decrease in both species below their peaks at 6-9 cmbsf. SMM 800-II (PC64) showed a similar sulfate profile, reaching its minimum by 3-4 cmbsf, with values measured at ~3 mM to the base of the short core at 9 cmbsf (Fig. 4B). Similarly, this drop was accompanied by a steep rise in porewater methane and sulfide, although as with SMM 800-I, we observed a subsequent drop in concentration below the 3-4 cmbsf horizon. At SMM 800-III (PC43), also collected in a sulfur-oxidizing microbial mat (Fig. S3), the peak in AOM activity also occurred at shallower depths (4-5 cmbsf), and, distinct from SMM 800-II, sulfate concentration dropped below detection below this depth (Fig. 4C). At SMM 863 (LC66), only porewater sulfate concentrations were measured. However, compared to the seep areas at SMM 800, we observed a much deeper penetration of sulfate into the sediment, dropping below detection by 21-24 cmbsf in this microbial mat habitat, suggestive of a lower methane flux (Fig. 4D).

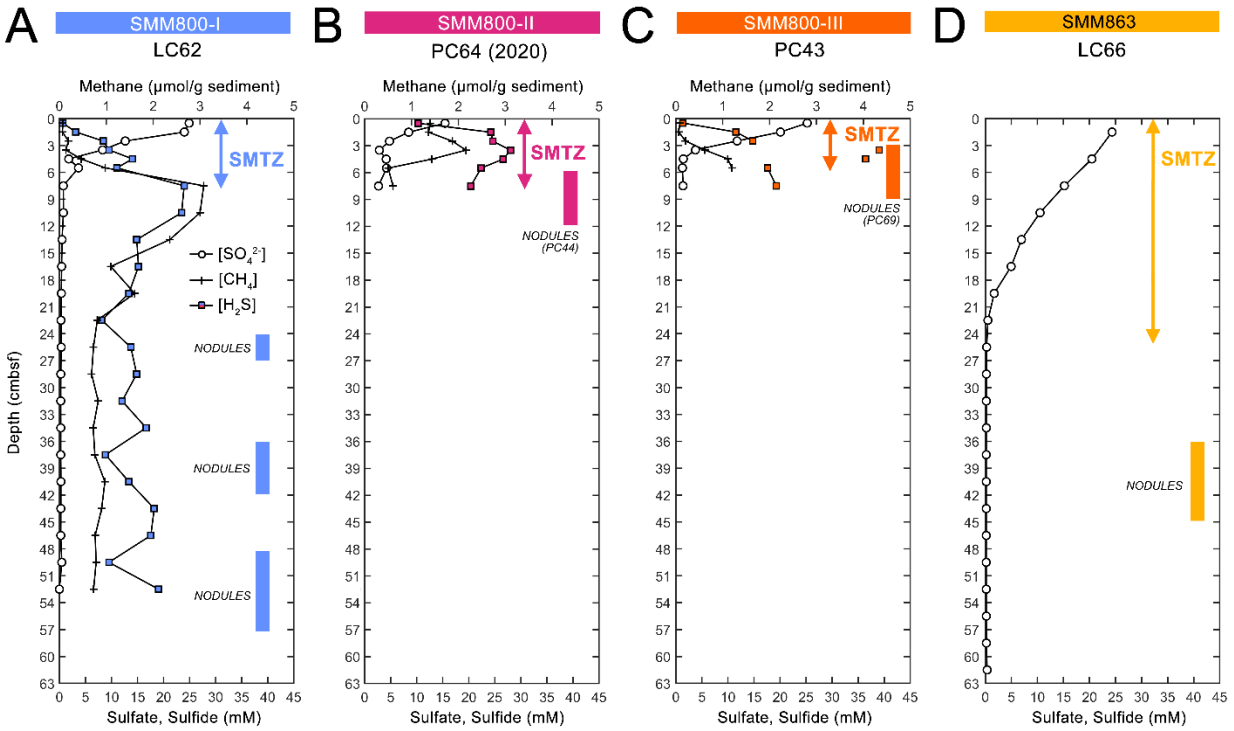


**Fig. 4** – Sulfate, methane, and sulfide concentration profiles collected for sediment porewaters at the seep areas (A-D) investigated in this study. We plot the median depth in centimeters below seafloor (cmbsf), where concentrations represent 3-cm depth horizons. The sulfate-methane transition zones (SMTZ), as determined by near-complete(<<1mM) sulfate drawdown in each core, are also demonstrated with colored arrows. Colored bars represent the horizons where nodules were recovered for further analysis. Nodules recovered from a different, co-located core at the seep area are also specified. PC64 from SMM 800-II was collected a year previously. We note that there are greater uncertainties with measured sulfide concentrations above the detection limit (>25mM, e.g., in PC43 from SMM 800-III). Only sulfate porewater concentration was collected for the core at SMM 863.

Porewater concentrations and the $\delta^{13}C$ values of dissolved inorganic carbon (DIC, $\delta^{13}C_{pw}$) in addition to the inorganic carbon isotopic concentration of the nodules ($\delta^{13}C_{nod}$) were also measured across the four areas in this study (Fig. 5). These data provide additional information into active AOM horizons where highly $^{13}C$-depleted bicarbonate is produced during methane oxidation and subsequently serves as the source of precipitation of authigenic carbonates (36). At SMM 800-I (LC62), porewater DIC concentrations steeply increased from <10mM to as high as ~42mM in the shallow subsurface (0-6 cmbsf) before stabilizing down core. Interestingly, this occurred in two distinct stages at SMM 800-I, which experienced a second rise in DIC to ~36mM at 15-18 cmbsf to the base of the core at 54 cmbsf (Fig. 5A). At both SMM 800-I and

SMM 800-III (PC43), this shallow spike in DIC concentration was paired with the peak in negative $\delta^{13}C_{pw}$, reaching values as low as -59.20‰, followed by a steady increase in $\delta^{13}C$ values down core. This indicated a peak in AOM in the shallow sediment horizons, consistent with the depth of the sulfate minima. SMM 800-II (PC64) exhibited a different trend, with comparatively less $\delta^{13}C_{pw}$ (-46.24‰, Fig. 5B). Notably, both DIC concentration and $\delta^{13}C_{pw}$ increased with depth, perhaps reflective of a mixture of both heterotrophic sulfate reduction and AOM at this site (37, 38). In comparison, $\delta^{13}C_{nod}$ exhibited a wide range of values across all four seep areas (-30.09‰ to -53.79‰). Notably, nodules from shallower depths at both SMM 800-I and SMM863 had greater $^{13}C$ enrichment than the nodules recovered deeper in the cores, where the $\delta^{13}C_{nod}$ at SMM 800-I was slightly more $^{13}C$-depleted (-46.03‰) than its surrounding porewater (-41.26‰).

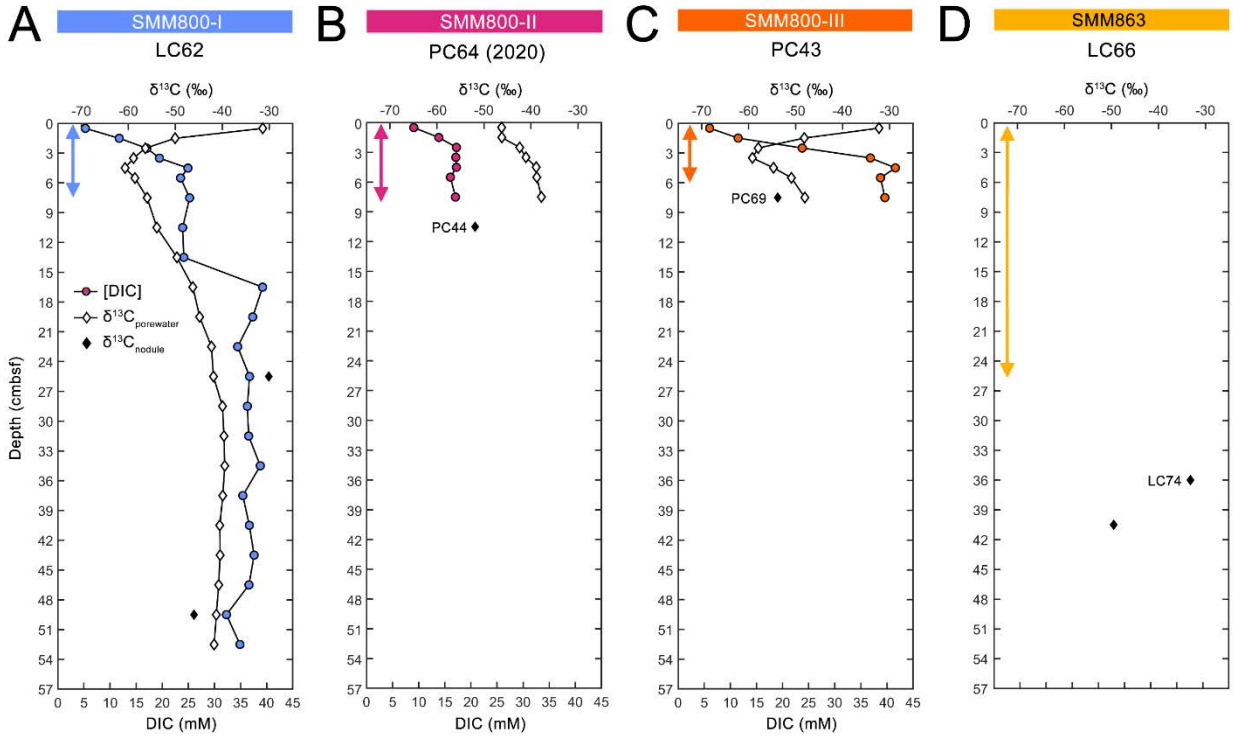


**Fig. 5** – Sediment porewater DIC, $\delta^{13}C_{porewater}$, and $\delta^{13}C_{nodule}$ profiles collected at the seep areas investigated in this study. We plot the median depth in centimeters below seafloor (cmbsf), where values represent multiple depth horizons. Because of the <3‰ spread between $\delta^{13}C_{nodule}$ replicates, values are simply averaged for comparison (individual values are included in Table S2). Colored arrows indicate an estimate for the location of the SMTZ, as in

Fig. 4. PC64 from SMM 800-II was collected a year previously. Only $\delta^{13}C_{nodule}$ was able to be collected for the cores at SMM 863.

**16S rRNA gene comparison of phylum-level diversity in nodules and host sediments**

Dominant microbial phyla across all sampled sediment and nodules (Fig. S6-S12) broadly resembled reports from other carbonate-bearing methane seep environments from Hydrate Ridge, OR and Eel River Basin, CA, which were often dominated by members of the *Halobacteriota* (putative methane-oxidizers largely affiliated with ANME archaea lineages), *Euryarchaeota*, and *Desulfobacterota* phyla (14, 16, 22). Additionally, members of the archaeal *Thermoplasmatota*, *Asgardarchaeota*, and *Crenarchaeota* were consistently recovered above 1% relative abundance. Of the bacterial phyla, *Desulfobacterota* were consistently present, with additional representation by members of the *Chloroflexi* and *Caldatribacteriota* (the latter exclusively associated with JS1, Table S11), and occasional detection (>1%) of taxa belonging to the *Planctomycetota*, *Acidobacteriota*, and *Fermentibacterota*. Notably, members from the *Fermentibacterota,* first characterized in anaerobic digesters by (39), were only substantially recovered in three nodules (1.05-2.28% relative abundance) at both the SMM 800-II and SMM 800-III seep areas and rarely recovered (<<1%) within the associated host sediments (Fig. S9, S11).

**Similar 16S rRNA community profiles between sediments and nodules from shallow sediment horizons**

In the shorter push cores from seep areas SMM 800-II and 800-III, *Halobacteriota* lineages consistently present in seep sediments were ANME-1a, ANME-2b, and ANME-2c (Fig. 6). Interestingly, these lineages persisted past the shallow zone of sulfate depletion in these cores. ANME-2c relative abundances were largely consistent with depth through 9-12 cmbsf at both

SMM 800-II and 800-III. However, we observed contrasting patterns in ANME-2b and ANME-1a abundances. Deeper horizons in SMM 800-II (PC44) showed a drop in the relative abundance of ANME-2b, concurrent with an increase in ANME-1a below 6 cmbsf. In the cores from SMM 800-III (PC43 and PC69) however, ANME-2b relative abundance and comparatively less ANME-1a were recovered from the deeper horizons, although this trend was much weaker in PC69 (Fig 6C). Within the three nodules recovered from these push cores, the dominant *Halobacteriota* lineages largely resembled those of their parent sediment horizons, where notable exceptions include an enrichment of ANME-1a (>20%) in the nodules from PC44 at SMM 800-II. Still, Shannon-Wiener and Inverse Simpson indices based on archaeal 16S ASV proportional abundances (Table S3) showed that archaeal diversity was greater in the sediment communities from SMM 800-II and SMM 800-III than in the nodules.

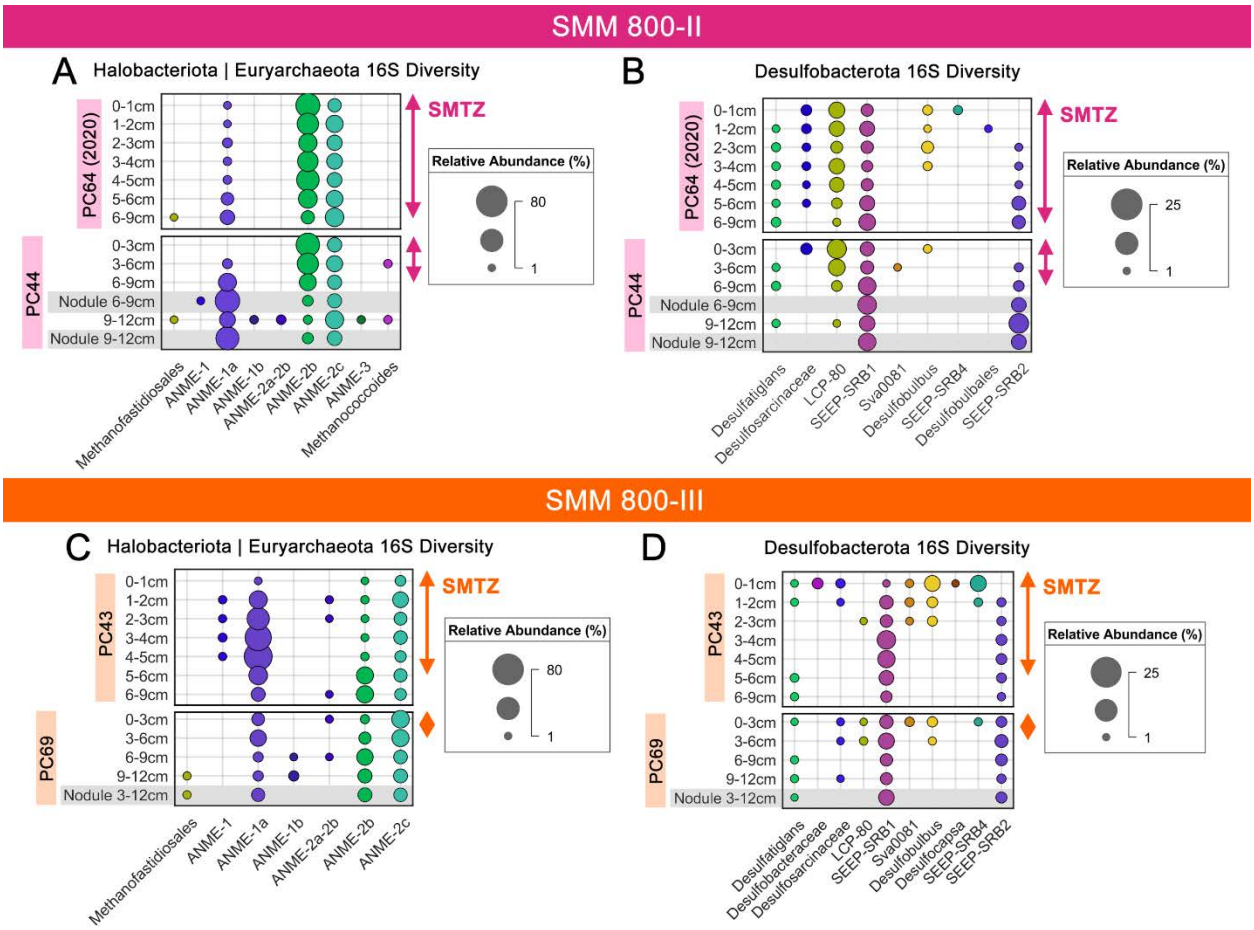


**Fig. 6** – Bubble plots summarizing the depth-resolved, 16S relative abundances for groups within *Halobacteriota* (featuring ANME), *Euryarchaeota (*featuring methanogens, e.g., *Methanofastidiosales*), and *Desulfobacterota* (featuring sulfate-reducing partners to ANME) in PC64 and PC44 at SMM 800-II (A, B), as well as PC43 and PC69 at SMM 800-III (C, D) . Where possible, ASVs within these phyla were grouped at the genus-level, or at the next highest taxonomic level possible, and then cut off below a minimum 1% relative abundance. Communities extracted from nodules are highlighted in grey and often represent larger depth horizons. The location of the sulfate-methane transition zone (SMTZ) according to porewater sulfate concentrations from the same or co-located sediment core is indicated with the colored arrows.

Dominant *Desulfobacterota* lineages within these shallow sediment horizons at SMM 800-II and 800-III included two main sulfate-reducing bacterial lineages, Seep-SRB1 and Seep-SRB2, that have been previously documented to form syntrophic associations with ANME (40–43), where their respective abundances appeared to covary with those of their ANME partners (Fig. 6BD). In the sulfate-rich, near-seafloor sediments (0-3 cmbsf) at both seep areas, a large diversity of other putative sulfate-reducing bacterial groups was also detected above 1%. These SRB lineages were largely affiliated with groups not known to directly participate in syntrophic AOM. By

comparison, *Desulfatiglans* (not currently known to be involved in AOM) was recovered from both seep areas at low abundances as deep as 12 cmbsf, including within the nodule from PC69 at SMM 800-III. While uncommon in seep ecosystems, this group has been observed in cold seep sediments in the Okinawa Trough that also harbor ANME-1 (29). Shannon-Wiener and Inverse Simpson indices based on bacterial 16S ASV proportional abundances (Table S3) indicated that the sediments surrounding the nodules from these seep areas had higher diversity, as found with the Archaea.

**Deeper sediment and nodule 16S rRNA surveys show persistence of *Halobacteriota* and *Desulfobacterota* and putative methanogenic lineages**

Similarly to SMM 800-II and 800-III, SMM 800-I (LC62) had a shallow SMTZ (sulfate depleted by 5-6 cmbsf) and both sediments and nodules were enriched in *Halobacteriota*, *Euryarchaeota*, and *Desulfobacterota* lineages within and well below the sulfate depletion depth. Archaeal diversity was largely dominated by ANME-1a (up to 66.5% relative abundance) which was recovered throughout the core at depths below 3 cmbsf. In the deeper horizons, this group was accompanied by ANME-1b at lower relative abundance (Fig. 7). Notably, within this long core, we also documented two distinct transitions in both archaeal and bacterial community composition, which occurred between 4-27 cmbsf and between 33-57 cmbsf, representing the base of the core.

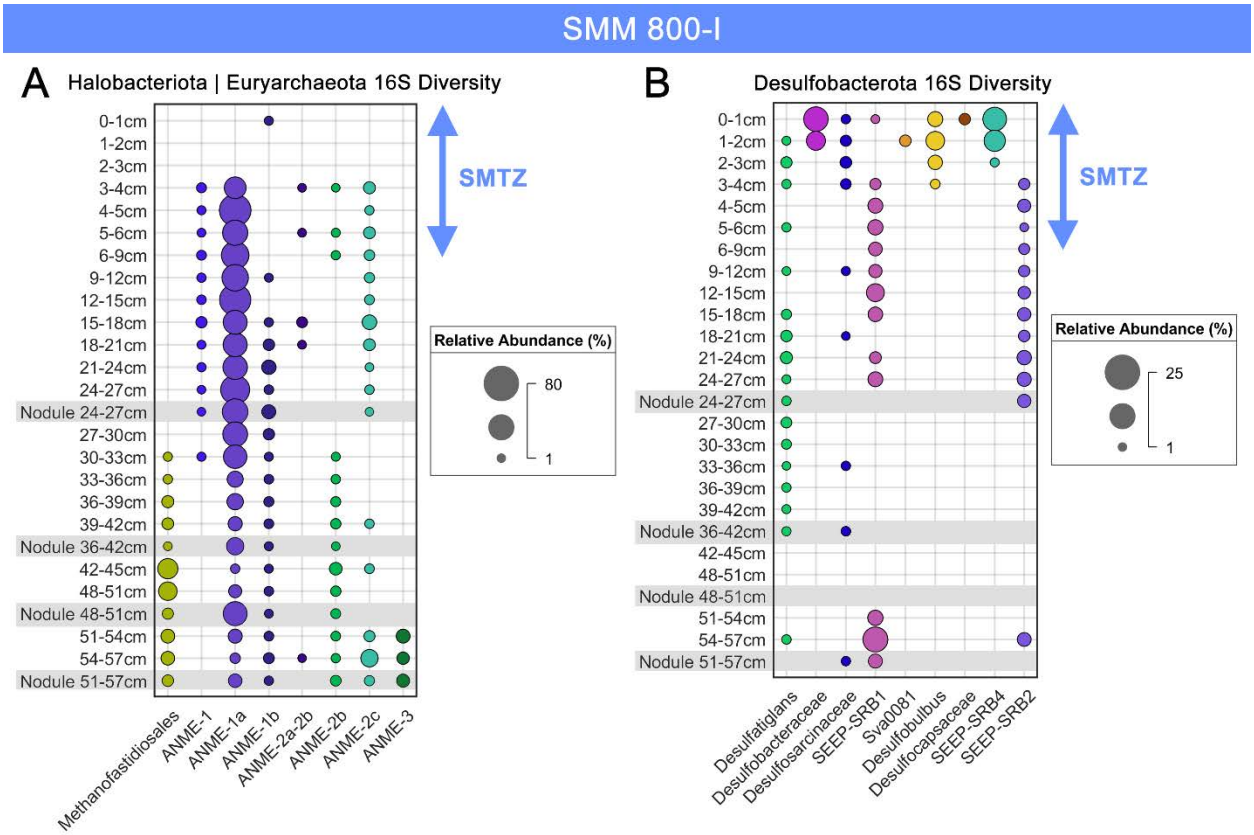


**Fig. 7** – Bubble plots summarizing the depth-resolved, 16S relative abundances for groups within *Halobacteriota*, *Euryarchaeota*, and *Desulfobacterota* in LC62 at SMM 800-I. Where possible, ASVs within these phyla were grouped at the genus-level, or at the next highest taxonomic level possible, and then cut off below a minimum 1% relative abundance. Communities extracted from nodules are highlighted in grey and often represent larger depth horizons. The location of the sulfate-methane transition zone (SMTZ) according to porewater sulfate concentrations from the same or co-located sediment core is indicated with the colored arrows. A) Relative abundances within prominent phyla *Halobacteriota* (featuring ANME) and *Euryarchaeota* (featuring methanogens such as *Methanofastidiosales*). B) Relative abundances within *Desulfobacterota* – the phylum with sulfate-reducing partners to ANME.

The first transition showed a shift from the consistent presence of ANME-2c (1-10% relative abundance), an unclassified ANME-1 lineage, and the putative syntrophic sulfate-reducing bacterial lineages Seep-SRB1 and Seep-SRB2 in the shallow sediment down to 27 cmbsf to an underlying zone ~24 cm thick where each of these groups, with the exception of sporadic occurrence of ANME-2c, were below detection (Fig. 7). The second transition, occurring between 33-57 cmbsf (well below the SMTZ), was marked by the emergence of ANME-2b and a putative methylotrophic methanogen lineage *Methanofastidiosales* (formerly the WSA2 group,

<20% relative abundance) largely dominated by a singular ASV (Table S11). The *Methanofastidiosales* are a poorly characterized group originally described from anaerobic sludge digesters (44) and observed in hydrothermal systems, gas hydrates, methane seeps, and methane-rich coastal sediments (29, 32, 45–48). This ASV was also detected above 1% abundance in the shallower push core sediments from SMM 800-II (PC464, PC44) and 800-III (PC69), including a nodule in PC69 (Fig. 6AC). A similar transition was observed for *Desulfobacterota* lineages, where the dominance of ANME partners Seep-SRB1 and Seep-SRB2 was succeeded by the persistent, though minor (<10%) presence of *Desulfatiglans* (Fig. 7B). Additional transitions in the archaeal and bacterial communities occurred in the uppermost 3 cm and deepest horizons of the core below 51 cmbsf, with the near seafloor sediments largely devoid of ANME lineages, but supporting a high diversity of *Desulfobacterota* not recovered in deeper horizons, including Seep-SRB4 and Desulfobulbus lineages, while the deepest horizons (51-54 cmbsf) showed an increase in *Halobacteriota* diversity, with the reappearance of members of the ANME-2c and detection of ANME-3, alongside the reoccurrence of Seep-SRB1. Compared to ANME-2c ASVs, the dominant Seep-SRB1 ASVs in the deepest core interval were different from the dominant ASVs in the intermediate depth horizons (3-27 cmbsf), although we observed a few shared Seep-SRB1 ASVs between these regions (Table S11).

Direct comparisons of the carbonate nodules (n=4) with paired sediments across these transitions revealed strong similarities between representative archaeal and bacterial taxa, including major members within *Halobacteriota* and *Desulfobacterota*, down to the ASV level (Fig. 7, Table S11). Beyond these taxa, both Shannon-Wiener and Inverse Simpson indices suggested the sampled nodule bacterial communities were consistently more diverse than their surrounding sediments, though this trend did not extend to the archaeal communities (Table S3).

The long cores recovered from SMM 863 revealed a slightly different community structure from SMM 800-I. Across both SMM 863 cores (LC74, LC66), we observed a clear transition in the dominant ANME and putative sulfate-reducing bacterial groups around 21-24 cmbsf (Fig. 8), aligned with the approximate depth of the SMTZ at this site. Here, members of the *Halobacteriota* above this transition zone were dominated by ANME-2c and known syntrophic partners belonging to the Seep-SRB1 as well as other uncharacterized lineages within the *Desulfosarcinaceae*. We also identified ANME-3 at varying abundances in the upper (<12 cmbsf) sediment in both cores. Below the transition at 21-24 cmbsf, ANME-2c was succeeded by lineages within ANME-1, primarily ANME-1b (up to 75% relative abundance). This transition corresponded with the appearance of the Seep-SRB2 lineage, previously observed to partner with ANME-1 (43, 49, 50). This depth distribution pattern was distinct from the other main ANME syntrophic partner, Seep-SRB1, which was consistently detected above 1% throughout both cores (Fig. 8B). Interestingly, we observed another transition in both cores, beginning at 36-39 cmbsf in LC74 and at 42-45 cmbsf in LC66, where ANME-2c reappeared alongside ANME-3. Here, the lower abundance of ANME-2c at depth was represented by the same dominant ANME-2c ASVs recovered in the upper sediment, while the ANME-3 ASVs at depth largely differed from those recovered near the top of the core (Table S11). Nodules sampled from this transition (n=3) revealed similar ANME-1b and ANME-1a lineages as in the surrounding sediments, down to the ASV level (Fig. 8A, Table S11), but lacked consistent representation from the other minor ANME lineages, including the uncharacterized ANME-1 group (in LC66) and ANME-2c (in both LC66 and LC74). Similarities were notably less apparent among the *Desulfobacterota*, where lineages present in the host sediment were often

absent from the nodules (i.e., Seep-SRB1 and Seep-SRB2) and lineages not observed in the immediate sediment horizon were observed in the hosted nodule (e.g., *Desulfatiglans* in LC66).

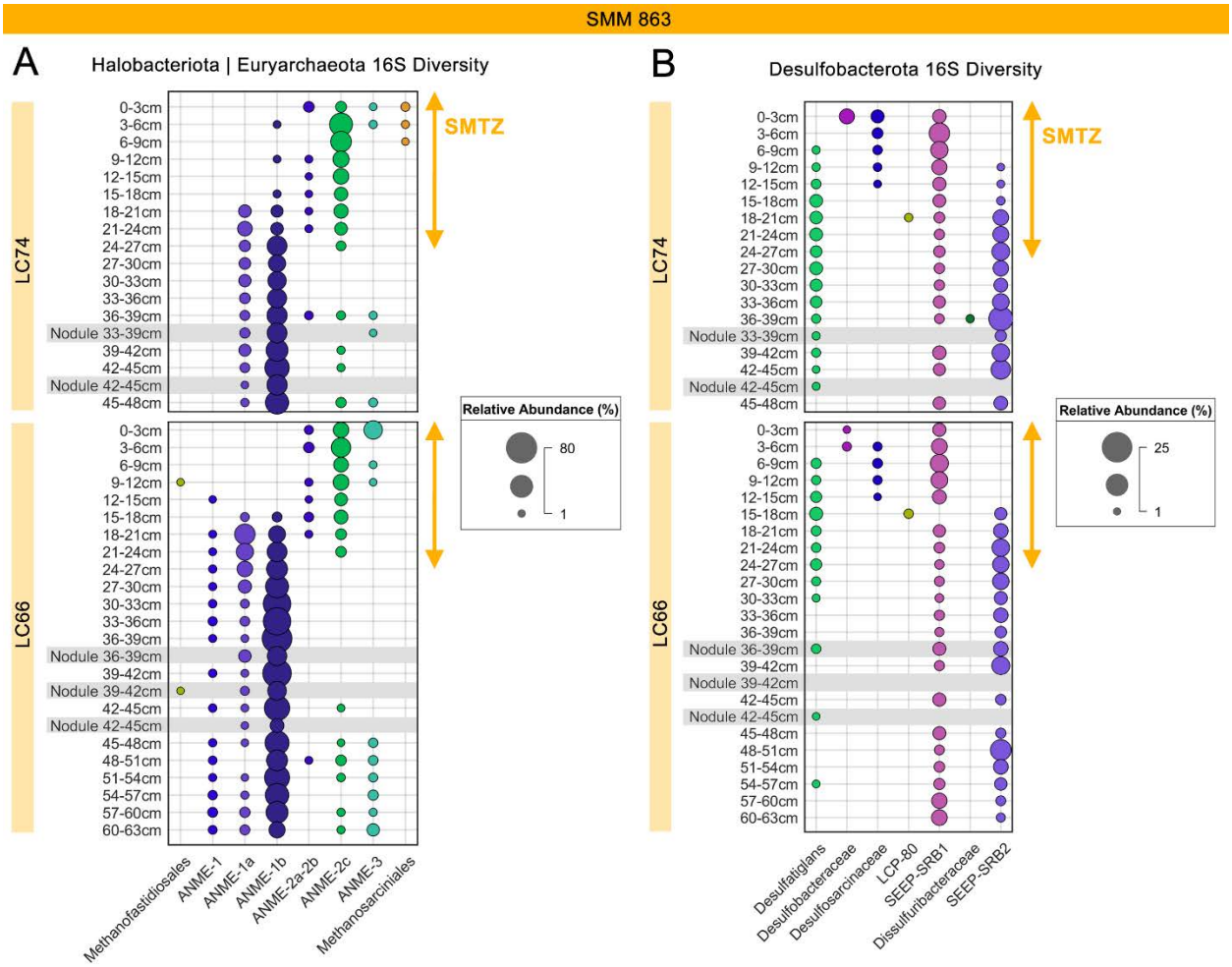


**Fig. 8** – Bubble plots summarizing the depth-resolved, 16S relative abundances for groups within *Halobacteriota*, *Euryarchaeota*, and *Desulfobacterota* in LC74 and LC66 at SMM 863. Where possible, ASVs within these phyla were grouped at the genus-level, or at the next highest taxonomic level possible, and then cut off below a minimum 1% relative abundance. Communities extracted from nodules are highlighted in grey and often represent larger depth horizons. The location of the sulfate-methane transition zone (SMTZ) according to porewater sulfate concentrations from the same or co-located sediment core is indicated with the colored arrows. A) Relative abundances within prominent phyla *Halobacteriota* (featuring ANME) and *Euryarchaeota* (featuring methanogens such as *Methanofastidiosales*). B) Relative abundances within *Desulfobacterota* – the phylum with sulfate-reducing partners to ANME.

## Cell abundance and fluorescence *in situ* hybridization (FISH) in nodules and sediments

Quantification of SYBR Gold®-stained cells and cell aggregates (cell associations > 5 µm) extracts were consistently higher (often 1-2 orders of magnitude) in sediment compared with

nodules across the sites, with typical single cell abundances ranging between $10^6$-$10^7$ cells $mg^{-1}$ in sediments compared with $10^5$-$10^6$ cells $mg^{-1}$ in nodules (Table 3). While differences in cell abundance between sediments and nodules were observed, a substantial decrease in cell abundance between the deeper sediment horizons (e.g., 2.7 x$10^7$ at 54-57 cmbsf) compared with shallower depths (e.g., 3.59 x$10^7$ at 9-12 cmbsf) was not detected.

**Table 3**
Aggregate/single-cell/cell clump SYBR Gold counts in nodules and paired sediment horizons

| Seep Area | Core ID | Core Horizon (cmbsf) | Avg Single Cells per mg Sample | SE | Avg Aggregates per mg Sample | SE |
|---|---|---|---|---|---|---|
| SMM 800-I | LC62 | 36-39 | $9.53\times10^6$ | $3.69\times10^5$ | $8.00\times10^3$ | $1.58\times10^3$ |
| | | 39-42 | $1.30\times10^7$ | $4.05\times10^5$ | $1.02\times10^4$ | $1.60\times10^3$ |
| | | (Nodule) 36-42 | $3.89\times10^5$ | $1.86\times10^4$ | $5.65\times10^2$ | $1.73\times10^2$ |
| | | 51-54 | $2.98\times10^7$ | $2.36\times10^6$ | $4.63\times10^4$ | $6.63\times10^3$ |
| | | 54-57 | $2.70\times10^7$ | $2.18\times10^6$ | $3.11\times10^4$ | $1.89\times10^3$ |
| | | (Nodule) 51-57 | $5.11\times10^5$ | $1.73\times10^4$ | $2.56\times10^3$ | $2.78\times10^2$ |
| SMM 800-II | PC44 | 6-9 | $4.05\times10^7$ | $2.10\times10^6$ | $8.28\times10^4$ | $2.17\times10^4$ |
| | | (Nodule) 6-9 | $4.21\times10^5$ | $1.54\times10^4$ | $4.63\times10^3$ | $7.19\times10^2$ |
| | | 9-12 | $3.59\times10^7$ | $2.01\times10^6$ | $2.88\times10^4$ | $8.87\times10^3$ |
| | | (Nodule) 9-12 | $1.15\times10^6$ | $7.56\times10^4$ | $2.89\times10^3$ | $4.11\times10^2$ |
| SMM 800-III | PC69 | 3-6 | $5.50\times10^7$ | $3.78\times10^6$ | $3.62\times10^4$ | $9.54\times10^3$ |
| | | 6-9 | $4.42\times10^7$ | $2.64\times10^6$ | $4.14\times10^4$ | $1.61\times10^4$ |
| | | 9-12 | $3.97\times10^7$ | $1.84\times10^6$ | $3.63\times10^4$ | $1.24\times10^4$ |
| | | (Nodule) 3-12 | $1.09\times10^6$ | $6.52\times10^4$ | $1.77\times10^3$ | $2.38\times10^2$ |
| SMM863 | LC66 | 42-45 | $3.01\times10^7$ | 9.51×105 | $2.64\times10^4$ | $3.02\times10^3$ |
| | | (Nodule) 42-45 | $1.70\times10^6$ | $8.68\times10^4$ | 4.01×103 | $9.20\times10^2$ |
| | LC74 | 42-45 | $7.45\times10^6$ | $4.70\times10^5$ | $3.16\times10^4$ | $4.11\times10^3$ |
| | | (Nodule) 42-45 | $1.60\times10^6$ | $1.54\times10^5$ | $1.08\times10^4$ | $1.51\times10^3$ |

The spatial associations in aggregates and morphology of Bacteria, Archaea, and ANME-1 cells were also examined within the recovered nodules by fluorescence *in situ* hybridization (FISH); (Fig. 9). The persistence of highly auto-fluorescent material within the long cores from seep areas SMM 800-I and SMM 863 made it difficult to clearly discern a positive fluorescence signal

from FISH, however we were able to observe positive hybridization with the ANME-1 probe, supporting 16S rRNA results. Notably, we observed large aggregates with morphology consistent with ANME-SRB consortia reported from seep sediments at a higher frequency within nodules recovered from the shallower sediment horizons (< 9-12 cmbsf) at seep areas SMM 800-II and 800-III, compared to the nodules recovered from deeper sediment intervals at SMM 800-I and SMM 863, where the FISH signal from cells was dimmer and cell aggregates were more loosely bound in an exopolymeric matrix (Fig. 9FG, Fig. S14).

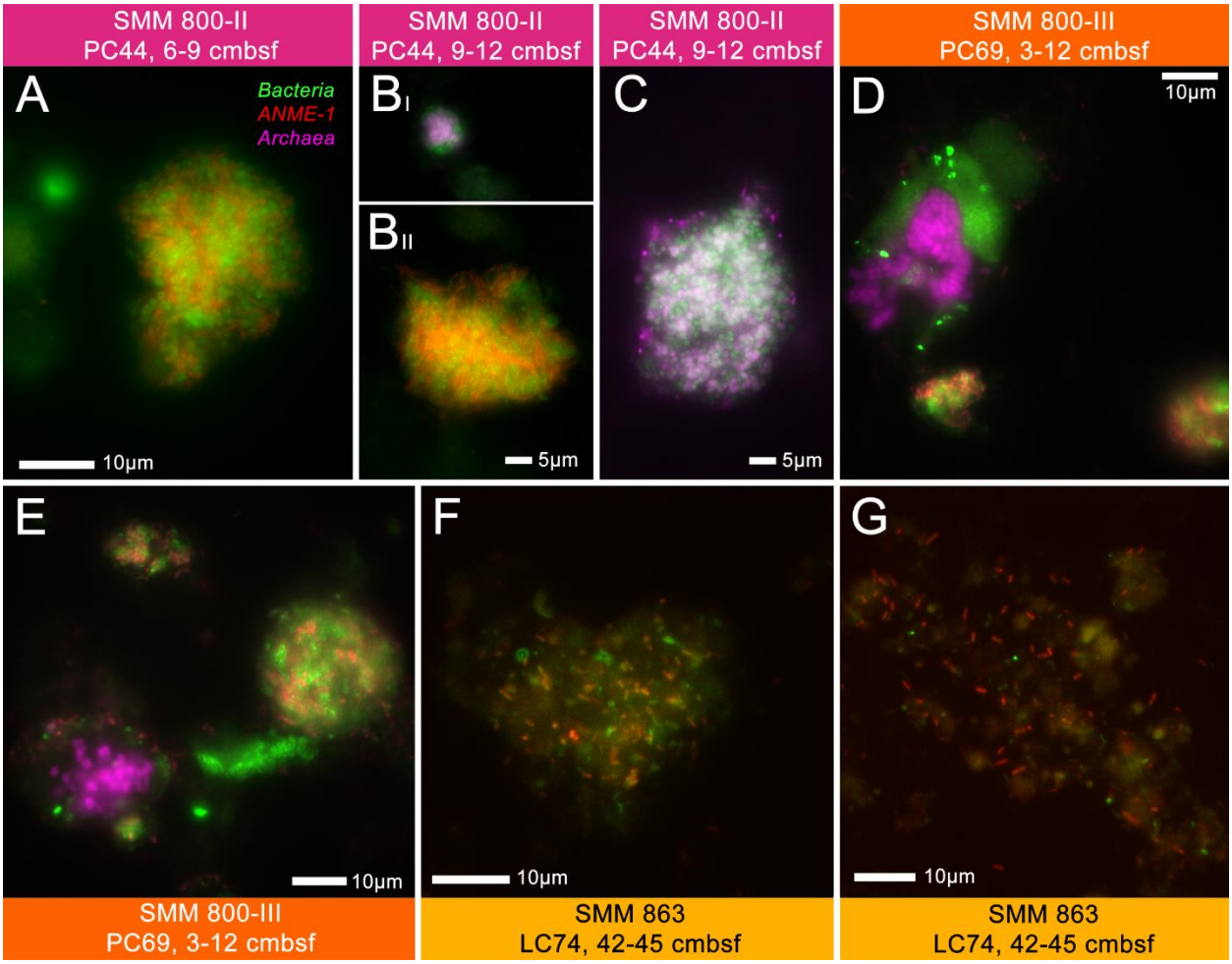


**Fig. 9** – Representative examples of carbonate nodule associated cells and aggregates recovered from SMM 800-II, 800-III, and 863, visualized by fluorescence in situ hybridization (FISH) using probes targeting *Bacteria* (EUB338 I-III, in green), ANME-1 (ANME1-350, ANME1-728; in red), and *Archaea* (ARCH915, in pink). Cell extracts for nodules from SMM 800-I were not shown due to strong interference from auto-fluorescent exopolymeric material.

**Single-cell translational activity measurements (BONCAT) show large shift in nodule endolithic activity between shallow sediments and deeper horizons below the SMTZ**

A subset of nodules (n=7) from 5 sediment cores were separated from their host sediment and incubated with the methionine analog HPG under sulfate- and methane-rich conditions to examine translational activity by endolithic microorganisms using biorthogonal noncanonical amino acid tagging (BONCAT), e.g., (49, 51, 52). Nodules were recovered after a 14-week incubation at 4ºC, and BONCAT analysis of carbonate-associated cells showed high heterogeneity in activity for both single cells and cell aggregates between nodules, ranging from less than 1% up to 39% of the recovered cells. The relative fraction of extracted cells and cell aggregates (>5 µm) with a confirmed BONCAT signal compared to those without is provided in Table 4. Representative examples of BONCAT stained cells and aggregates from each of the seep areas are shown in Fig. 10.

**Table 4**
Proportion of BONCAT-active cells to non-BONCAT-active cells from incubated nodules

| Seep Area | Core ID | Nodule Horizons (cmbsf) | BONCAT-Active Single Cells | BONCAT-Active Aggregates |
|---|---|---|---|---|
| SMM 800-I | LC62 | 36-42 | <1% (n = 765) | *no aggregates observed* |
| | | 51-57 | <1% (n = 767) | 0% (n=1) |
| SMM 800-II | PC44 | 6-9 | 39% (n = 792) | 60% (n = 10) |
| | | 9-12 | 14% (n = 1011) | 40% (n = 5) |
| SMM 800-III | PC69 | 3-12 | 4% (n = 1041) | 62% (n = 21) |
| SMM863 | LC66 | 42-45 | <1% (n = 1062) | *no aggregates observed* |
| | LC74 | 42-45 | 7% (n = 857) | 100% (n = 2) |

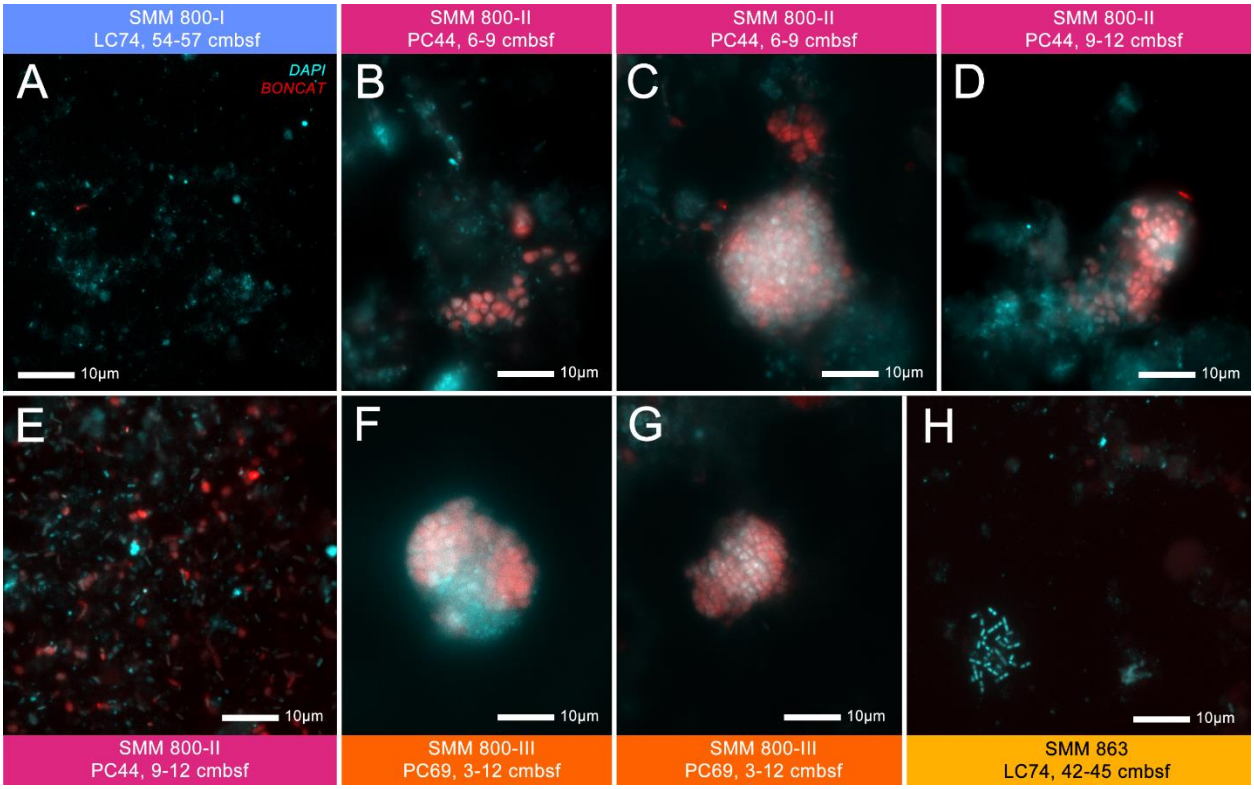


**Fig. 10** – Cell extracts from recovered carbonate nodules at all four seep areas, displaying the presence/absence of newly synthesized proteins with BONCAT (in red) after a 14-week incubation with methionine analog, L-Homopropargylglycine (HPG). DAPI staining of nucleic acids indicating cells is in cyan. Positive BONCAT signal was consistently observed in all extracts from the shallower nodules at SMM 800-II and 800-III, compared to the consistent lack of signal at SMM 800-I and 863.

Nodule-hosted cells recovered from SMM 800-I (LC62, 36-42 and 51-57 cmbsf, both well below the SMTZ), did not exhibit evidence of HPG assimilation among the >700 cells examined per sample. Additionally, these nodules lacked cell aggregates commonly found in shallower sediment horizons. The absence of a BONCAT signal aligns with the minimal sulfide production observed prior to the HPG incubation period (Fig. S15). We observed similar results with a deep nodule recovered from SMM863 below the SMTZ (LC66, 42-45 cmbsf). However, the nodule recovered from the parallel core (LC74) from the same depth horizon did show a weak BONCAT signal (7% of total cells screened) in single cells and aggregates, despite lack of observed sulfide production prior to HPG incubation (Fig. S15). This signal indicated that these endolithic habitats below the SMTZ continued to support viable microorganisms (Table 4).

The low microbial activity and lack of cell aggregates observed in the majority of nodule incubations from the deeper sediment intervals contrasted with the nodules recovered from the shallow horizons within the SMTZ (between 3-12 cm) at SMM 800-II and 800-III. Here, we observed active HPG assimilation for both single cells and cell aggregates, with up to 39% of the single cells (n=792) and 62% of aggregates (n=21) showing a positive BONCAT signal (Table 4). FISH-based identification of BONCAT positive cells indicated a large fraction of these active cells were Archaea (ARCH915 probe, Fig. S16). These samples actively produced sulfide prior to the incubation, reaching values as high as 8 mM after 30 days (Fig. S15), supporting their likely involvement in sulfate-coupled methane oxidation.

## Discussion

In this study, increased depth sampling directly within active seeps using ROV-deployed long cores provided a window into microbial community transitions within and below the SMTZ. We sampled seven sediment cores containing carbonate nodules directly within microbial mat-associated, active seep habitats from four seep areas associated with two carbonate mounds in the Santa Monica Basin. The three seep areas at SMM 800 showed consistent geochemical profiles with high, sulfate-coupled AOM activity characterized by a shallow (<9 cmbsf), sharply defined SMTZ, whereas the two long cores from SMM 863 instead revealed a much deeper (~21 cmbsf) sulfate depletion zone suggestive of lower methane flux and AOM activity (21). Carbonate nodules recovered from all four seep areas across these distinct geochemical zones enabled us to investigate the physical properties, along with the diversity and metabolic activity of nodule-hosted microbial communities relative to their host sediments, with implications for

464 the degrees to which these incipient carbonate nodules preserve records of past AOM and
465 continue to serve as habitats for *in situ* endolithic communities.
466
467 **Closely-linked sediment and nodule-hosted microbial communities indicate ongoing**
468 **exchange throughout and below the SMTZ**
469 16S rRNA-based community profiles from recovered nodules at all the characterized seep areas
470 reinforced a close similarity to those of their host sediments, regardless of depth and
471 geochemical regime. Non-metric multidimensional scaling (NMDS) ordination of all sediment
472 and nodule-derived ASVs (Fig. S13) also showed a consistent, area-specific clustering between
473 nodules and sediments. This coupling generally agrees with previous studies comparing various
474 carbonate substrates, including nodules, from seep sites at Hydrate Ridge, OR; Eel River Basin,
475 CA; and the Sea of Japan (14–16, 22).
476 Collectively, these shared microbial community profiles across major geochemical transition
477 zones are strong evidence of continuous colonization and response to *in situ* conditions which
478 collectively influence nodules and sediments, rather than a time-integrated, microbial
479 'thumbprint' of the surrounding sediment.
480 This is further supported by the high open porosities measured for the nodules in this study,
481 regardless of depth and pore size distributions (< 350 μm), which likely facilitate continuous
482 colonization by surrounding seep sediments. Indeed, 13-month seafloor colonization experiments
483 of sterilized carbonate substrates within and on the periphery of deep-sea methane seeps
484 previously demonstrated active colonization by seep sediment microorganisms, including
485 ANME-1 (16). Although the mechanisms of potential exchange between nodules and sediments
486 remain unknown — especially since motility has not been definitively observed in ANME —

previous studies have hypothesized the involvement of fluid advection and/or methane ebullition in facilitating active carbonate colonization (14, 16, 53, 54).

Further, the high nodule open porosities support sufficient connectivity for methane and sulfate perfusion, along with the diffusion of small organic molecules (e.g., HPG, used in BONCAT experiments). As such, these nodules likely experience very similar, current geochemical pressures as the surrounding sediments, which supports the shared microbial community transitions observed in both sediments and nodules from SMM 800 and SMM 863. Indeed, subsurface methane fluxes can vary over periods that can last from days to centuries (55–57), where changes in geochemical stratification exert an active role in structuring the sediment microbial communities performing AOM and facilitating authigenic carbonate precipitation (1, 14, 36, 58–60).

Isotopic and mineral signatures from the nodules recovered below the SMTZ also record carbonate precipitation in different geochemical regimes from the present environments observed. Despite being a sulfate-depleted environment, the consistently depleted $\delta^{13}C$ values for these nodules — below that of marine organic carbon, -25‰ (61) — support at least a partly AOM-driven origin, and thus preclude exclusive precipitation under the current geochemical conditions. Indeed, all the nodules at SMM 800-I were aragonite-rich (78.2-85.2%), suggestive of a history largely informed by shallower, sulfate-bearing sediments (62, 63). By contrast, the greater Mg-calcite content (45.1-65.1%) in the nodules from SMM 863 support a longer-lived interval in a deeper, more sulfate-limited AOM environment (6, 59, 64, 65). Together, these data suggest that the nodules recovered at depth are likely to have experienced microbial community shifts to reflect communities better adapted to *in situ* conditions, which agrees with a model of continued colonization from the surrounding sediments.

510 **Persistence of ANME lineages suggest potential adaptation or survival under sulfate-poor**
511 **conditions below SMTZ**

512 Long cores collected from both SMM 800-I and SMM 863 revealed the consistent dominance of
513 ANME-1 lineages over ANME-2 in the deeper sulfate-depleted sediments and nodules,
514 consistent with several previous studies that have noted this general pattern in seep ecosystems
515 worldwide (24, 26, 28, 30–32, 66, 67). The occurrence of ANME-1 lineages well below the
516 SMTZ, frequently representing the same ASVs as those found within zones of high AOM
517 activity, may reflect thus greater physiological plasticity among this archaeal lineage.

518 Interestingly, the difference in community profiles below the SMTZ between SMM 800-I
519 (LC62) and SMM 863 (LC74, LC66) attests to additional environmental factors driving niche
520 differentiation in seep sediments and nodules in this geochemical zone. While the dominance of
521 ANME-1b below the SMTZ at SMM 863 may be linked in part to AOM with known ANME
522 partners Seep-SRB1 and Seep-SRB2, the low abundance (<1%) of *Desulfobacterota* sequences
523 below the SMTZ at SMM 800-I suggest that the ANME-1a cells at depth may persist without a
524 sulfate-reducing partner. FISH data from several environments have documented the occurrence
525 of ANME-1 as single cells without an attached bacterial partner (23, 66, 68–71), further
526 supportive of ANME-1's metabolic flexibility beyond sulfate-coupled AOM.

527 Notably, the occurrence of putative methylotrophic methanogens within the
528 *Methanofastidiosales* at depth supports the transition to a methanogenic regime below the
529 SMTZ, where ANME-1a and *Caldatribacteriota* (exclusively JS1, Table S11) were found to co-
530 occur. JS1 has been previously identified in anaerobic and/or methanogenic seep sediments
531 worldwide (16, 26, 72–74), and hypothesized to participate in hydrocarbon degradation that may
532 supply key substrates for methanogenesis (44, 73–75). Indeed, it has also been hypothesized that

at least some members of the ANME-1 may be capable of methanogenesis (31, 70, 76–80). Although porewater methane concentrations do not conclusively support methane production, previous methane measurements at SMM 800 (33) do support a biological origin for methane, based on the purity and isotopic signature (-70.8‰ $\delta^{13}C$). Similarly, the observed rise in porewater DIC and associated $\delta^{13}C$ in the deeper sediment horizons at SMM 800-I (LC62) may be explained by $^{13}C$-enriched DIC produced during methanogenesis (81, 82). Enriched $^{13}C$ content associated with an increased dolomite fraction in a deeper nodule from SMM 800-I (LC62, 24-27 cmbsf) also agrees with carbonate formation in historically methanogenic sediment regimes below the SMTZ (6, 64) — a phenomenon additionally observed for a sub-SMTZ nodule recovered from SMM 863 (LC74, 33-39 cmbsf).

Beyond methanogenesis, the observed co-occurrences of ANME-1 lineages, *Methanofastidiosales*, and JS1 may also attest to Fe-coupled AOM below the SMTZ at SMM 800-I. Fe-coupled AOM has been observed in sulfate-depleted marine sediments (29, 83–91), where explicit associations between ANME-1a/1b, JS1, and *Methanofastidiosales* have been statistically supported within seep sediments likely hosting Fe-AOM (29). Further, the detection of ANME-3 in the lower (51-57 cmbsf) horizons of core LC62 at SMM 800-I aligns with observations of ANME-3 in sulfate-depleted marine sediments and microcosms supporting Fe-AOM (83, 85). Ultimately, lack of dissolved iron concentrations for the sediment or discernible iron mineral content in the nodules precludes geochemical support for Fe-AOM at SMM 800-I. Still, past observations of this metabolic regime and its connection to frequently observed microbial taxa in globally-distributed seep sediments below the SMTZ — including sediments and nodules at the seep areas in this study — suggest that the extent of AOM below the SMTZ at active seeps may be under-constrained.

More broadly, the co-occurrence of both ANME/SRB and methanogenic lineages at SMM 800-I may also suggest *in situ* mixing of AOM and methanogenic regimes. These regimes have been hypothesized to co-occur in marine sediments (92) and have been reported for sediments in the Bothnian Sea (87). Significant correlations between ANME clades and methanogen groups from sulfate-depleted sediments at the Okinawa Trough have also suggested a degree of cryptic methane cycling (29). Collectively, these studies underscore the complexity of resolving distinct metabolic regimes in seep sediments.

Interestingly, the weaker-to-negligible BONCAT signal in incubated nodules from below the SMTZ at SMM 800-I and SMM 863 under sulfate and methane-replete conditions indicates that substrate concentrations alone may be insufficient to stimulate measurable AOM activity in nodules at depth over the time period of the incubation (3.5 months). This was despite recovering high cell abundances that included both single cells and aggregate morphologies consistent with ANME (including FISH-detectable ANME-1) in the deeper nodules. Together, these data suggest that measuring metabolic activity for incubated nodules recovered at depth may require longer observation periods, or more sensitive measurements.

In this regard, the minimal activity observed for carbonate nodules below the SMTZ may be compared to that of seafloor carbonates in low-activity seep areas. Indeed, *in situ* experiments transplanting seafloor-exposed carbonates from low to high activity seepage areas by (16) reported shifts towards microbial community structures enriched in lineages involved in AOM and sulfur-based metabolisms after 13 months. Further, sulfide measurements from incubated low activity seafloor carbonates in (11) showed that reactivation of AOM in hosted endolithic communities could take months to years. By contrast, previous $^{14}CH_4$ radiotracer measurements of methane oxidation rates from low-activity seep carbonates, incubated under similar

conditions, showed detectable, if low methane oxidation (<200 nmol after 7 days) after the introduction of AOM-favorable conditions (8).

Collectively, these data may also point to the understudied nature of metabolic dormancy in seep microbial communities. Previous studies have diverged on interpretation of gene-based profiles of seep sediments and buried seep carbonates, where relict, or 'fossil' DNA has been proposed to persist in marine sediments (93–95) and cited in buried seep carbonate crusts (58, 59, 90), such that community profiles are not representative of metabolically viable cells. However, recent studies have suggested that 'fossil' DNA negligibly affects taxonomic surveys of environmental samples, especially in marine sediments below the bioturbation zone and even across systems where physical protection of DNA (e.g., seep carbonates) may generate bias (96, 97). As such, we consider 16S rRNA-based nodule community profiles to largely reflect the intact cell assemblage observed in nodules from all depths, with clear variation in metabolic activity with increasing depth below the SMTZ, representing a mixture of dormant and active microorganisms within this endolithic habitat.

Future investigations at methane seeps should therefore seek to better characterize the role of AOM in both the sediment and nodules below the SMTZ, which remains poorly understood. Longer (>1 year), lab-based studies examining the dynamics and range of metabolisms leveraged in these methane-rich, sulfate-poor conditions may shed additional information on factors driving metabolic activity in low-energy seep environments and how sensitive these communities are to the types of geochemical changes characteristic of transient methane seep activity.

**Mechanisms, timescales for sediment community entrapment or exchange in nodules remain underexplored**

Although continued exposure and exchange between seep nodules and sediments is strongly supported by the observations presented in this study, the processes or conditions that may act to decouple the nodule environment from its surroundings remain to be more clearly defined. Minor offsets observed between sediment and nodule communities in NMDS ordination of all sediment and nodule-derived ASVs (Fig. S13) may reflect subtle substrate-level differences in community structure. Further, we observed higher community richness in shallow sediments compared to nodules at SMM 800-II and 800-III (Table S3). This trend has also been observed previously in methane seeps at Hydrate Ride, OR (14, 22), and may suggest a local environment more favorable to certain microbial taxa. Indeed, lower cell and cell aggregate abundances in the nodules from SMM 800 and SMM 863 relative to the surrounding sediments may result from niche-specific differences and/or likelihood of some barriers to free exchange between sediments and porous carbonate nodules.

Minor discrepancies between sediment-nodule pairs have also been hypothesized to originate from translocation events that disrupt the original emplacement of incipient seep carbonates. These translocation events act on a local basis and may be driven by sudden gas hydrate decomposition or ebullition events (14). Still, the prevalence of this phenomenon is not known, as the formation and depositional history of seep nodules remains poorly constrained. Sediment-hosted seep carbonates are thought to be continuously subject to burial by continuous sediment transport from nearby coasts, uplift from tectonic movements or gas hydrate accumulation (6, 33, 64), and dissolution from nearby sulfide oxidation and/or aerobic methane oxidation (98–103). In addition to precipitation dynamics, these forces are all expected to shape the duration and nature of exchange between sediments and hosted carbonate nodules in ways that outline future paths of investigation. Although the ages of the nodules in this study remain unconstrained (though

loosely estimated at $10^2$-$10^3$ years, (33)), the data presented in this study suggest that over the interval since their formation, diagenetic forces have not acted to significantly decouple sediment and nodule microbial communities.

Additional sampling of seep sediment-hosted nodules should seek to more clearly define the time-constrained formation and diagenetic history captured by these understudied carbonates relative to their surrounding sediments, especially in instances where nodule-hosted microbial communities and surrounding sediment communities differ. Uranium-thorium (U-Th) dating, combined with $\delta^{13}C$ and X-ray diffraction (XRD) characterizations of these sediment-hosted carbonates can better address their age, provenance, and subsequent diagenetic history. In turn, these studies can advance our understanding of controls informing continued microbial habitation in seep sediment-hosted nodules.

## Conclusions

In this study, we integrated microbiological and geochemical analyses of paired seep carbonate nodules and host sediments spanning the SMTZ and below at two previously described seep sites in the Santa Monica Basin, CA. We extend prior characterizations of seep sediment-hosted nodules with this integrated analysis, mapping changes in nodule-hosted microbial community structure and activity of these endolithic microorganisms across steep geochemical and microbiological transitions. By sampling within and below the SMTZ, we captured similar community transitions in both nodules and sediments, suggestive of continued perfusion and exchange between nodules and surrounding sediments, regardless of geochemical conditions. Porosity and mineralogy measurements also indicated sediment-nodule connectivity was feasible and had likely persisted throughout the nodule's formation, regardless of formation environment.

Unique community structures beneath the SMTZ also attested to different metabolic regimes captured in both sediments and nodules, with the potential for co-occurrence of methanogenesis and AOM. Still, BONCAT activity measurements under sulfate/methane-rich conditions showed that the deeper nodules collected below the SMTZ were slow or no longer capable of producing measurable evidence of AOM within the 14-week incubation period compared to nodules from near-seabed horizons supporting active, sulfate-coupled AOM. Future investigations should explore the range of AOM and non-AOM metabolisms feasible in seep sediment ecosystems in wider detail and seek to more accurately constrain the range of diagenetic histories captured by seep nodules to better constrain the past and current degree of AOM activity recorded in these endolithic habitats.

## Materials and Methods

### Sample collection

Sediment cores were collected with the manipulator arm using the *ROV Doc Ricketts* during dives DR1329 and DR1333 during the WF05-21 Southern California cruise on the *R/V Western Flyer*. Additionally, we included data from one core (PC64) collected on dive DR1248 by ROV *Doc Ricketts* at SMM 800 in February 2020 during the WF02-20 Southern California cruise on the *R/V Western Flyer*. Additional information on site contexts and additional sample recovery details may be found in the Supplemental Material. A further detailed summary of all the sediment and nodules in the study is also included in Table S10.

Upon recovery, all cores were kept in a 4°C walk-in cooler until processing. Within hours of collection, sediment cores were documented and sectioned shipboard into 1- or 3-cm horizons by upward extrusion. Nodules were manually identified during core sectioning and kept within the

associated sediment horizons. These horizons were then bagged in sterile Whirl-Pak bags, sealed in Ar-flushed Mylar bags (IMPAK Corporation), and maintained in cold storage at 4°C for, and during, transport to the laboratory.

In the laboratory (<2 weeks after sample collection), nodules >1cm in diameter were manually extracted from the bagged, anoxic sediment horizons under $N_2$ and rinsed three times in 0.22 µm-filtered, 3X phosphate-buffered saline (PBS, as in (104)) to remove any adhered sediment. After rinsing, nodules from each horizon were then sub-sampled for various physical, geochemical, microbiological analyses (further detailed by section titled in the Supplemental Material). Due to limited sample available for multiple analyses, some nodules were combined across adjacent sediment horizons and treated as the representation of a larger segment of the sediment core collected (Table S10). We conducted a second cleaning step for the rinsed nodules used for DNA-based community analysis and visualization by fluorescence microscopy to minimize sediment contamination following the optimized protocol for DNA extraction from carbonate nodules described in (14). In (14), rigorous testing for sufficient removal of surface contamination from the sediment hosted nodules was tested using *E. coli* as a tracer, with the following protocol demonstrating complete removal of DNA from the exogenously introduced microbes. Briefly, this surface treatment included additional rinses with cold, 0.22 µm-filtered 3X PBS, sonication, and centrifugation (additional details are provided in the Supplemental Material). Rinsed nodules designated for activity measurements with bioorthogonal non-canonical amino acid tagging (BONCAT) (51) were immediately transferred to separate, sterile, acid-washed media bottles, submerged in cold, 0.22 µm-filtered, $N_2$-sparged artificial seawater (media composition available in Supplemental Material Table 1.10), and stoppered with an acid-treated butyl rubber stopper (Th. Geyer GmbH & Co. KG). After immersion, bottle headspaces

were flushed with pure $CH_4$ for 1 minute with a needle and then pressurized to 2 bar. Samples were incubated in the dark at 4°C.

**Methane measurements**

On both the WF05-21 and WF0-20 cruises, sediment methane samples were collected by 1 mL cut off syringe from each sediment core horizon and immediately transferred into 3 mL of 5M NaOH in a pre-weighed gas-tight 10 mL Restek vial, shaken to mix, and then stored upside down at room temperature until analysis. In the laboratory, methane concentrations in the headspace of the vials were measured with a Hewlett Packard (HP) 5890 Series II Plus Gas Chromatography system with a flame ionization detector, connected to a HP 7694 Headspace Sampler with a 1 mL sample loop. The GC column was a 30 m HP-Plot/Q column with inner diameter (I.D.) of 0.32 mm. The software used for analysis was Agilent GC ChemStation (version A.09.03 [1417]). A calibration series ranging from 250 ppm (v/v) to 5000 ppm (v/v) was run immediately prior to samples using lab grade $CH_4$ gas (100%) injected into sealed 10 mL Restek vials using a gas-tight syringe. Methane volumetric ppm values were converted to µmol assuming ideal gas behavior at standard temperature and pressure. These values were normalized relative to the mass of sediment added to the Restek vials during the cruise, where masses were corrected for porosity by weighing sediment from each horizon before and after drying in an oven.

**Sulfate measurements**

On both cruises, sediment porewater was collected in pressure-driven ‘squeezers’ (105), using argon to compress the sediment section against a 47 mm, 0.22 µm polycarbonate filter (Thermo Fisher) to recover sediment-free porewater in gas-tight, 60 mL syringes while minimizing

717 exposure to air. Porewater from each sediment horizon was then filtered through a 0.22 µm
718 polyethersulfone (PES) syringe filter (Tisch) into 2 mL Eppendorf tubes and stored at -20°C for
719 later analysis. In the laboratory, the concentration of major ion species (e.g. sulfate) was
720 determined by ion chromatography at the Resnick Sustainability Institute's Water and
721 Environment Lab at the California Institute of Technology. Specifically, samples were run on a
722 250 mm Dionex IonPac instrument (Thermo Fisher) with AS19-4µm and CS16-4µm columns for
723 anions and cations, respectively — each with 50 mm versions as guard columns. 100 µL of each
724 porewater sample were diluted 50x in milliQ ultrapure DI water (final volume 5 mL) before
725 running. Standard curves were generated using calibration standards diluted similarly to samples,
726 with 100 µL of 500 mM NaCl added to mimic typical seawater sample peak behavior. Analyte
727 peaks were automatically integrated and major ion species, including sulfate, were automatically
728 calculated using the prepared standards with the Chromeleon Dionex IC (Thermo Fisher, v7.2.9)
729 software, with manual inspection to ensure regular peak shapes.
730
731 **Sulfide measurements**
732 Samples for porewater sulfide concentrations were prepared by the addition of 0.5mL of 0.22 µm
733 filtered porewater from each sediment horizon to 0.5 mL of 0.5M zinc acetate in a 1.5 mL
734 Eppendorf tube to precipitate zinc sulfide. Due to its lability, sulfide samples were processed first
735 after porewater collection from the squeezer apparatus. In the laboratory, the precipitated sulfide
736 was quantified spectrophotometrically according to the Cline sulfide assay protocol (106).
737 Briefly, this involved the acidification of the sample and reaction with N, N-dimethyl-p-
738 phenylenediamine dihydrochloride in presence of ferric chloride. The resulting methylene blue
739 solution's absorbance was measured in duplicate at 670-nm wavelength with a microplate reader

(Sunrise, Tecan). Concentrations were calculated after subtracting absorbance values from DI $H_2O$ blanks from concurrently measured zinc sulfide standards prepared from sodium sulfide solutions (0.12 mM to 25 mM). We additionally measured 10x and 50x dilutions to allow for quantification of highly sulfidic samples within the linear color range.

**DIC and $\delta^{13}C$ analyses**

We measured dissolved inorganic carbon (DIC) concentrations and its $\delta^{13}C$ in porewater ($C_{pw}$), as well as the $\delta^{13}C$ of nodule ($C_{nod}$) where sufficient porewater or nodule material allowed. After extraction and rinsing, nodule samples were air dried and ground to a fine powder with an agate mortar and pestle, which was cleaned with DI water and ethanol between samples. Replicate subsamples of powdered nodules (0.45-0.65-mg) were added to 12 mL, acid-washed and combusted Exetainer vials (Labco). The vials were then flushed with helium for 2 minutes and acidified with 200 µL 43.5% phosphoric acid. To measure porewater DIC and $\delta^{13}C_{pw}$, 1 mL of extracted porewater was immediately added via syringe to 12 mL, acid-washed and combusted Exetainer vials (Labco) pre-flushed with helium and pre-loaded with 100 µL 43.5% phosphoric acid during the WF05-21 and WF02-20 cruises. In the laboratory, the released $CO_2$ gas was measured on a GasBench II coupled to a Delta V Plus isotope ratio mass spectrometer (IRMS) at the Stable Isotope Facility at the California Institute of Technology.

Concentrations of DIC were determined based on comparison of the average total peak area of sample injections to replicate sodium bicarbonate standard curves. The 6-point dilution standard curves for the porewater DIC used ultrapure DI $H_2O$ as a background standard and a solution series (1, 2.5, 5, 10, 20, and 30mM) of sodium bicarbonate (-2.9‰).

$\delta^{13}C_{nod}$ and $\delta^{13}C_{pw}$ values were corrected for instrument dependency on $CO_2$ concentration and then normalized to the VPDB scale with a two-point calibration (107) using the Merck ($\delta^{13}C$ = -49.2‰) and Carrara Marble (CM 2013, $\delta^{13}C$ = +2‰) carbonate standards. Here, we use solid carbonate powder isotope standards for both $\delta^{13}C_{nod}$ and $\delta^{13}C_{pw}$ on the basis of a quantitative conversion (i.e., total carbonate consumption) and since O isotopes are not considered for this study.

**Nodule porosity & porosimetry**

During nodule sub-sampling, select nodules (where sufficient material allowed) were additionally rinsed in deionized water to remove any salts and dried at room temperature for structural and mineralogical analysis. To characterize the internal structure of the recovered carbonate nodules, we determined their open porosity using a water intrusion (or Archimedes) method. We followed Method A of ASTM D792 (108), which collects the dry mass, the immersed mass (i.e., mass of fluid displaced), and the saturated mass (i.e., mass of fluid-saturated object) of a nodule sample with DI water, according to Eq. 1:

$$\mu_a = \frac{(m_3 - m_1)}{(m_3 - m_2)} \times 100 \quad (1)$$

where $\mu_a$ is the apparent, or open, porosity (expressed as a percentage of the sample bulk volume), $m_1$ is the dry mass, $m_2$ is the immersed mass, and $m_3$ is the saturated mass. This was achieved with a density apparatus attached to a fine scale (Mettler Toledo). Additionally, we measured the pore size distribution of paired samples with Hg-porosimetry. This method uses a pressurized, non-wetting liquid (mercury) to intrude the nodule pore spaces, where the cumulative volume of intruded mercury is recorded at each pressure interval, corresponding to a certain pore size (109). We used a Micromeritics AutoPore IV Mercury Intrusion Porosimeter to

785 measure open pore size distribution between 6 and 350 µm by recording cumulative mercury
786 intrusion volume at 90 intervals within a pressure range of 3.51 and 206 kPa.
787
788 **XRD**
789 Nodule subsamples for mineralogical characterization with X-ray diffraction (XRD) were air-
790 dried and ground to fine powder with an agate mortar and pestle, cleaned with ethanol between
791 each use. Resulting powders were analyzed with a Rigaku SmartLab powder diffractometer at
792 the X-Ray Crystallography Facility in the Beckman Institute at the California Institute of
793 Technology. We used a Cu Kα source at 50 kV and 40 mA. Scans were run from 5° to 70° 2θ at
794 a scanning speed of 0.02° 2θ/s. Rigaku SmartLab Studio II was used to fit and identify peaks and
795 the 2020 Crystallography Open Database was used for phase identification. The relative semi-
796 quantification of clearly identifiable phases was calculated according to the reference intensity
797 ratio (RIR) based on a corundum standard and documented in weight percent. For the phases, the
798 RIR method used the (104) peak heights of calcite, Mg-calcite and dolomite, the (111) peak
799 height of aragonite, and the (101) peak height for quartz. Here, Mg-calcite corresponds to
800 $(Ca_{0.9}Mg_{0.1})O_3$, as measured by (35).
801
802 **16S rRNA gene sequencing**
803 To characterize and compare the diversity and composition of the microbial communities across
804 the seep areas represented in the dataset, we sequenced the V4 and V5 regions of the 16S rRNA
805 gene. Here, 2mL of sediment from each core horizon was sampled by sterile 1 mL cutoff
806 disposable syringe into a 2 mL screwcap Eppendorf tube and immediately stored at -80°C for
807 DNA extraction. In the laboratory, doubly rinsed nodules intended for sequencing were also

finely ground and frozen at -80°C after extraction from sediment and cleaning as described above. DNA was extracted from 0.15-0.3 g (wet weight) of thawed sediment or finely ground nodule powder using the DNeasy PowerSoil Pro Kit (Qiagen). Target sequences were then amplified with a 2-step Illumina sequencing strategy (110). Briefly, this involved an initial amplification with 515f (5'-TCGTCGGCAGCGTCAGATGTGTATAAGAGACAG-GTGYCAGCMGCCGCGGTAA-3') and 926r (5'-GTCTCGTGGGCTCGGAGATGTGTATAAGAGACAG-CCGYCAATTYMTTTRAGTTT-3') primers, followed by a second amplification to include the necessary Illumina barcodes prior to being sequenced.

Adapters from paired-end sequences were removed using 'Cutadapt' (v2.9), (111). Trimmed reads were then input into QIIME2 (v2020.11), (112), where we used a DADA2 pipeline (v1.14.1), (113) to filter and denoise the reads as well as remove chimeric sequences. ASVs with assigned taxonomy were generated from the merged, non-chimeric sequences in QIIME2 using the Silva V138.1 SSURef database feature classifier (114). Classified, non-zero ASVs for all the sediment and nodules in the study are included in Table S11. Additional details on modified DNA extraction protocols, PCR amplification, gene sequencing, and read processing are also included in the Supplemental Material.

During subsequent analysis, we calculated Shannon-Wiener and Inverse Simpson diversity indices for archaeal and bacterial ASVs from the carbonate nodules and their host sediments. Further information on how these indices were calculated are detailed in the Supplemental Material. Additionally, we performed a non-metric multidimensional scaling (NMDS) ordination of all carbonate nodule and sediment-derived ASVs. Further details on how this ordination was performed is also detailed in the Supplemental Material.

831

832 **Fluorescence in situ hybridization (FISH)**

833 During sediment core sectioning, 0.5-0.7 mL sediment per horizon was immediately added to 0.5
834 mL of a 0.22 µm filtered 4% paraformaldehyde solution in 3X PBS and fixed overnight at 4°C.
835 Afterwards, the sample was washed twice with 0.22 µm filtered 1X PBS and then re-suspended
836 in a 50% ethanol: 1X PBS medium and stored at -20°C. During nodule extraction in the
837 laboratory, doubly rinsed nodules were finely ground with a sterile agate mortar and pestle.
838 Immediately after grinding, the ground nodules were also fixed and washed as was done for the
839 sediments, but re-suspended in a 70% ethanol: 1X PBS medium prior to storage at -20°C. To
840 visualize the cells with minimal interference from sediment and mineral particles, we then
841 performed a density separation using percoll, based on a modified protocol outlined in (8, 23,
842 115). Briefly, 100-200 µL fixed sediment or carbonate was added to 400 µL of a chilled, 0.22 µm
843 filtered 'combination' buffer made of 0.5% v/v Tween 20, 3 mM sodium pyrophosphate, and
844 0.35% wt/v PVP (116). Samples were then sonicated on ice over 3 cycles at amplitude 20 on a
845 Q55 sonicator (Qsonica), with 10 seconds of active sonication and 10 seconds of rest in between
846 to avoid overheating. Next, sample tubes were shaken on a vortex mixer (Vortex-Genie 2,
847 Scientific Industries) for 30 minutes at room temperature. We then added 400 µL of chilled, 0.22
848 µm filtered 1X PBS before mixing and overlaying the mixed sample on 950 µL of a chilled
849 percoll density gradient. The gradient tubes were then centrifuged at 18,000 x g for 25 minutes at
850 4ºC (Microfuge 18, Beckman Coulter). After centrifugation, the density gradient supernatant was
851 transferred to a new set of sample tubes and centrifuged again at 16,000 x g for 3 minutes at 4ºC
852 to form cell pellets. The pellets were washed twice with 0.22 µm filtered 1X PBS.

853 The washed cells were then stained with a SYBR® Gold (Thermo Fisher) solution at a 25X final
854 concentration in ultrapure DI $H_2O$ in the dark for 15 minutes at room temperature. After staining,
855 the cells were centrifuged at 16,000 x g for 3 minutes at room temperature, re-suspended in
856 ultrapure DI $H_2O$, and stored overnight at 4ºC. The next day, the cells were mounted via vacuum
857 filtration onto a 0.2 µm black polycarbonate filter and a 5µm PVDF backing filter (Millipore
858 Sigma). The filters were washed twice in ultrapure DI $H_2O$, air dried, and then stored in the dark
859 at 4ºC until counting. Prior to coverslip placement, each filter received ~ 50 µL
860 Vectashield® Antifade Mounting Medium (VectorLabs). For counts, we used an Olympus BX51
861 fluorescence microscope using a 100x objective lens (Olympus). Thirty fields of view per
862 filtered sample were surveyed to determine the number of cell aggregates and single cells. For
863 these counts, any association of cells larger than 5 µm were considered aggregates. Cell and
864 aggregate counts were normalized per unit dry mass for all sample types.
865 To observe the presence and morphologies associated with particular taxa, we used fluorescence
866 in situ hybridization (FISH). For FISH, the washed, percoll-extracted cells were re-suspended in
867 ultrapure DI $H_2O$ and stored overnight at 4ºC. The following day, cell suspensions were dried at
868 room temperature onto separate 6 mm wells on PTFE- and L-lysine-coated glass slides (Tekdon).
869 The hybridization probes EUB338 [5'-GCTGCCTCCCGTAGGAGT-3' (117), 3' conjugated
870 Alexa Fluor™ 488 dye], EUB338 II [5'- GCAGCCACCCGTAGGTGT-3' (118), dual-labeled
871 Alexa Fluor™ 488 dye], EUB338 III [5'- GCTGCCACCCGTAGGTGT-3' (118), dual-labeled
872 Alexa Fluor™ 488 dye], ANME1-350 [5'-AGTTTTCGCGCCTGATGC-3' (19), dual-labeled
873 Alexa Fluor™ 546 dye], ANME1-728 [5'- GGTCTGGTCAGACGCCTT-3', designed using
874 ARB (119) to hit the ANME1 Clade of the Silva 138.1 database), 5' conjugated Alexa Fluor™
875 546 dye], and ARCH-915 [5'-GTGCTCCCCCGCCAATTCCT-3' (120), dual-labeled Alexa

876 Fluor™ 647 dye] were used for the mounted cell extracts. The hybridization probe mix was
877 prepared in sterile, 40% formamide concentration, with final concentrations of 5-ng/µL for each
878 probe (Integrated DNA Technologies). Each well on the slide then received 10 µL of probe mix
879 and was hybridized in the dark, overnight at 46°C. The next day, the glass slides with hybridized
880 cells were immersed and incubated in a pre-warmed hybridization wash in the dark for 10
881 minutes at 48°C. The slides were then rinsed in ultrapure DI $H_2O$ and allowed to air dry (in the
882 dark) completely. FISH hybridization probe and wash recipes are provided in Tables S4-S5.
883 Prior to coverslip placement, each well also received 10 µL of a 90% Citifluor™ mounting
884 medium (Electron Microscopy Sciences) with 4.5 ng/µL 4',6-diamidino-2-phenylindole (DAPI)
885 for nucleic acid visualization. Hybridized cells were then visualized with an ELYRA S.1 / Axio
886 Observer Z1 super resolution microscope using a 100x objective lens (Zeiss). For control
887 experiments, each glass slide had a well with mounted cells subjected to the entire FISH protocol
888 but used ultrapure DI $H_2O$ instead of probes. For these wells, negligible signal was observed.
889

890 **Single cell translational activity measurements with BONCAT**

891 Translational activity was observed by amending a subset of the bottled nodules with an anoxic
892 L-Homopropargylglycine (HPG) solution. HPG works as a methionine analog and is
893 incorporated during protein synthesis without significantly altering community composition or
894 metabolic activity (49, 51, 52). After incorporation, proteins containing HPG can be
895 fluorescently labeled through copper-catalyzed azide-alkyne 'click' chemistry, which enables
896 detection via fluorescence microscopy (49, 52, 121, 122).
897 In this study, the nodules previously maintained in $N_2$-sparged artificial seawater with a 2 bar
898 $CH_4$ headspace were separated into replicate experimental and control bottles. Where possible,

899 the nodules were selected to minimize mass differences between experimental and control
900 groups. Each new sterile, acid-washed bottle received 50 mL of 0.22 μm-filtered, $N_2$-sparged
901 artificial seawater of the same composition (Table S6, sufficient to immerse the nodules).
902 Throughout transfer and immersion, all bottles were constantly maintained under active $N_2$ flow
903 to minimize oxygen exposure. After immersion, all bottle headspaces were flushed with pure
904 $CH_4$ for 1 minute and pressurized to 2 bar. Samples were then incubated in the dark at 4°C for a
905 period of 5 weeks, during which the media was periodically sampled to monitor sulfide
906 concentrations in control and experimental bottles. After determining comparable sulfide
907 production between each control and experimental group (Fig. S15), the artificial seawater media
908 was replaced with freshly prepared 0.22 μm-filtered, $N_2$-sparged artificial seawater. Additionally,
909 each experimental bottle received aqueous 0.22 μm-filtered, $N_2$-sparged HPG to a final
910 concentration of 200 μM. Throughout media replacement and HPG addition, all bottles were
911 constantly maintained under active $N_2$ flow to minimize oxygen exposure. After immersion, all
912 bottle headspaces were again flushed with pure $CH_4$ for 1 minute and pressurized to 2 bar.
913 Samples were then incubated in the dark at 4°C for a period of 14 weeks to ensure sufficient
914 HPG assimilation.
915 At the end of the incubation period, nodules from both control and experimental bottles were
916 ground, fixed, and washed as previously described for FISH hybridization. Cells from each
917 fixed, ground nodule were then extracted and mounted onto separate 6 mm wells on PTFE- and
918 L-lysine-coated glass slides as previously described. For the BONCAT dye click reaction, the
919 glass-mounted cell extracts were then dehydrated by sequential immersion in 50% (1 minute),
920 80% (3 minutes), and 90% (3 minutes) ethanol: DI $H_2O$ baths and dried room temperature.

921 We used BONCAT azide dye Oregon Green 488 (VectorLabs) at a final concentration of 20 µM.
922 10-µL of the dye solution was then added to each well and incubated in the dark for 30 minutes.
923 For the incubation, we flushed a lidded sample container with Ar, in which we placed the
924 mounted cells to minimize oxygen exposure, which can reduce the fluorescent signal. After
925 incubation, the slides were washed in 0.22 µm-filtered 1X PBS for 10 minutes (in the dark),
926 quickly rinsed in ultrapure DI $H_2O$, and allowed to air dry in the dark prior to FISH
927 hybridization. Hybridization probes EUB338 [5' conjugated cyanine 3 dye], EUB338 II [3'
928 conjugated cyanine 3 dye], EUB338 III [5' conjugated cyanine 3 dye], and ARCH-915 [dual-
929 labeled Alexa Fluor™ 647 dye] were used. Hybridization was done at 35% formamide. Washing
930 and addition of DAPI-Citifluor® mounting medium was performed as previously described.
931 BONCAT click reaction and FISH hybridization recipes are listed in Tables S7-S9.
932 Click-dyed, hybridized cells were then visualized with an ELYRA S.1 / Axio Observer Z1 super
933 resolution microscope using a 100x objective lens (Zeiss). Fraction of cells with HPG signal
934 were evaluated by counting HPG-incubated, extracted cells with observable signal above a mean
935 background threshold calculated from the control cells' auto-fluorescence in the same channel.
936 For FISH and BONCAT control experiments, each glass slide had a well with mounted, non-
937 HPG labeled cells subjected to the entire FISH protocol but used ultrapure DI $H_2O$ instead of
938 probes. For these cells in these negative control wells, a negligible signal was observed.
939

940 **Data availability**

941 The Santa Monica Mounds Low Altitude Survey System (LASS) survey was done in the Spring
942 of 2018 using *ROV Ventana* on *R/V Rachel Carson*. The Santa Monica Mounds Mapping AUV

surveys were done multiple times from *R/V Zephyr* and *R/V Carson*. Featured grids and photomosaics will be available at MGDS https://www.marine-geo.org/.

The raw DNA sequence reads generated from the SMM 800 sediment cores in this study were initially submitted to NCBI under project accession number PRJNA1196099 (sample accession numbers: SAMN45814414-SAMN45814434; SAMN45814441- SAMN45814448) and are accessible at https://www.ncbi.nlm.nih.gov/bioproject/ PRJNA1196099. The rest of the raw DNA sequence reads generated for this study (SMM 800 nodules, SMM 863 samples, experimental controls) were submitted to NCBI under accession numbers PRJNA1207588 and accessible at https://www.ncbi.nlm.nih.gov/bioproject/PRJNA1207588.

## Acknowledgements

We are indebted to the captain, crew, and pilots of the *ROV Doc Ricketts* from the WF05-21 cruise, who made this work possible. We also thank David Caress, Charles Paull, Eric Martin, and the Autonomous Systems Operations group at the Monterey Bay Aquarium Research Institute (MBARI), as well as the crews of *R/V Zephyr* and *R/V Carson* for collection, processing, and analysis of bathymetry maps of the Santa Monica Basin. We thank S. Lim (University of Nevada, Las Vegas), J.S. Magyar (Caltech), and S. Goffredi (Occidental College) for their help in sample collection and processing during the WF05-21 Southern California cruise of the *R/V Western Flyer*, S. Connon (Caltech) for technical support and barcoding of 16S amplicons for sequencing, D. Utter (Caltech) and H. Sapers (Northern Arizona University) for support during data processing.

S.A. Parra and V.J. Orphan conceptualized the study and acquired financial support for the study. J. Mullahoo analyzed dissolved porewater methane. L.K. Quinn analyzed nodule open porosity and Hg-porosimetry. R.L. Wipfler analyzed porewater sulfate concentrations. S.A. Parra processed and analyzed all other data presented in the study, including nodule selection, porewater sulfide measurements, DIC/$\delta^{13}$C measurements, x-ray diffraction, DNA extraction, 16S rRNA sequence analyses, fluorescence microscopy, and BONCAT incubations. M.J. Mayr and V.J. Orphan supervised the study. S.A. Parra wrote the original draft and incorporated edits before and during the publication stage. M.J. Mayr, J. Mullahoo, L.K. Quinn, R.L. Wipfler, and V.J. Orphan all participated in critical review and commentary on the paper draft before and during the publication stage.

This work was supported in part by NASA's Interdisciplinary Consortia for Astrobiology Research (ICAR) program under Award Number AWD-005316-G4 (to V.J. Orphan), the National Science Foundation under Award Number 2048666 (to V.J. Orphan), and NASA's Future Investigators in NASA Earth and Space Science and Technology (FINESST) program under Award Number 80NSSC22K1336 (to S.A. Parra). This material is based upon work supported by the U.S. Department of Energy, Office of Science Biological and Environmental Research Program under Award Number DE-SC0022991 (to V.J. Orphan).

Disclaimer: This report was prepared as an account of work sponsored by an agency of the United States Government. Neither the United States Government nor any agency thereof, nor any of their employees, makes any warranty, express or implied, or assumes any legal liability or responsibility for the accuracy, completeness, or usefulness of any information, apparatus, product, or process disclosed, or represents that its use would not infringe privately owned rights. Reference herein to any specific commercial product, process, or service by trade name,

trademark, manufacturer, or otherwise does not necessarily constitute or imply its endorsement, recommendation, or favoring by the United States Government or any agency thereof. The views and opinions of authors expressed herein do not necessarily state or reflect those of the United States Government or any agency thereof.

## References

1. Reeburgh WS. 2007. Oceanic Methane Biogeochemistry. Chem Rev 107:486–513.

2. Boetius A, Wenzhöfer F. 2013. Seafloor oxygen consumption fuelled by methane from cold seeps. 9. Nature Geosci 6:725–734.

3. Aharon P, Schwarcz HP, Roberts HH. 1997. Radiometric dating of submarine hydrocarbon seeps in the Gulf of Mexico. GSA Bulletin 109:568–579.

4. Peckmann J, Thiel V. 2004. Carbon cycling at ancient methane–seeps. Chemical Geology 205:443–467.

5. Teichert BMA, Bohrmann G, Suess E. 2005. Chemoherms on Hydrate Ridge — Unique microbially-mediated carbonate build-ups growing into the water column. Palaeogeography, Palaeoclimatology, Palaeoecology 227:67–85.

6. Naehr TH, Eichhubl P, Orphan VJ, Hovland M, Paull CK, Ussler W, Lorenson TD, Greene HG. 2007. Authigenic carbonate formation at hydrocarbon seeps in continental margin sediments: A comparative study. Deep Sea Research Part II: Topical Studies in Oceanography 54:1268–1291.

7. Haas A, Peckmann J, Elvert M, Sahling H, Bohrmann G. 2010. Patterns of carbonate authigenesis at the Kouilou pockmarks on the Congo deep-sea fan. Marine Geology 268:129–136.

8. Marlow JJ, Steele JA, Ziebis W, Thurber AR, Levin LA, Orphan VJ. 2014. Carbonate-hosted methanotrophy represents an unrecognized methane sink in the deep sea. 1. Nature Communications 5:5094.

9. Marlow J, Peckmann J, Orphan V. 2015. Autoendoliths: a distinct type of rock-hosted microbial life. Geobiology 13:303–307.

10. Marlow JJ, Hoer D, Jungbluth SP, Reynard LM, Gartman A, Chavez MS, El-Naggar MY, Tuross N, Orphan VJ, Girguis PR. 2021. Carbonate-hosted microbial communities are prolific and pervasive methane oxidizers at geologically diverse marine methane seep sites. PNAS 118.

11. Mayr MJ, Parra SA, Connon SA, Narayanan AK, Murali R, Cremiere A, Orphan VJ. 2025. Distinct Microbial Communities Within and On Seep Carbonates Support Long-term Anaerobic Oxidation of Methane and Novel pMMO Diversity. bioRxiv https://doi.org/10.1101/2025.02.04.636526.

12. Lein AYu. 2004. Authigenic Carbonate Formation in the Ocean. Lithology and Mineral Resources 39:1–30.

13. Watanabe Y, Nakai S, Hiruta A, Matsumoto R, Yoshida K. 2008. U–Th dating of carbonate nodules from methane seeps off Joetsu, Eastern Margin of Japan Sea. Earth and Planetary Science Letters 272:89–96.

14. Mason OU, Case DH, Naehr TH, Lee RW, Thomas RB, Bailey JV, Orphan VJ. 2015. Comparison of Archaeal and Bacterial Diversity in Methane Seep Carbonate Nodules and Host Sediments, Eel River Basin and Hydrate Ridge, USA. Microb Ecol 70:766–784.

15. Yanagawa K, Shiraishi F, Tanigawa Y, Maeda T, Mustapha NA, Owari S, Tomaru H, Matsumoto R, Kano A. 2019. Endolithic Microbial Habitats Hosted in Carbonate Nodules Currently Forming within Sediment at a High Methane Flux Site in the Sea of Japan. 11. Geosciences 9:463.

16. Case DH, Pasulka AL, Marlow JJ, Grupe BM, Levin LA, Orphan VJ. 2015. Methane Seep Carbonates Host Distinct, Diverse, and Dynamic Microbial Assemblages. mBio 6.

17. Hoehler TM, Alperin MJ, Albert DB, Martens CS. 1994. Field and laboratory studies of methane oxidation in an anoxic marine sediment: Evidence for a methanogen-sulfate reducer consortium. Global Biogeochemical Cycles 8:451–463.

18. Hinrichs K-U, Hayes JM, Sylva SP, Brewer PG, DeLong EF. 1999. Methane-consuming archaebacteria in marine sediments. Nature 398:802–805.

19. Boetius A, Ravenschlag K, Schubert CJ, Rickert D, Widdel F, Gieseke A, Amann R, Jørgensen BB, Witte U, Pfannkuche O. 2000. A marine microbial consortium apparently mediating anaerobic oxidation of methane. Nature 407:623–626.

20. Orphan VJ, House CH, Hinrichs K-U, McKeegan KD, DeLong EF. 2001. Methane-Consuming Archaea Revealed by Directly Coupled Isotopic and Phylogenetic Analysis. Science 293:484–487.

21. Borowski W, Paull C, Ussler W. 1996. Marine Pore-water Sulfate Profiles Indicate in situ Methane Flux from Underlying Gas Hydrate. Geology 655–658.

22. Marlow JJ, Steele JA, Case DH, Connon SA, Levin LA, Orphan VJ. 2014. Microbial abundance and diversity patterns associated with sediments and carbonates from the methane seep environments of Hydrate Ridge, OR. Front Mar Sci 1.

23. Orphan VJ, House CH, Hinrichs K-U, McKeegan KD, DeLong EF. 2002. Multiple archaeal groups mediate methane oxidation in anoxic cold seep sediments. Proceedings of the National Academy of Sciences 99:7663–7668.

24. Orphan VJ, Ussler W, Naehr TH, House CH, Hinrichs K-U, Paull CK. 2004. Geological, geochemical, and microbiological heterogeneity of the seafloor around methane vents in the Eel River Basin, offshore California. Chemical Geology 205:265–289.

25. Blumenberg M, Seifert R, Reitner J, Pape T, Michaelis W. 2004. Membrane lipid patterns typify distinct anaerobic methanotrophic consortia. Proceedings of the National Academy of Sciences 101:11111–11116.

26. Harrison BK, Zhang H, Berelson W, Orphan VJ. 2009. Variations in Archaeal and Bacterial Diversity Associated with the Sulfate-Methane Transition Zone in Continental Margin Sediments (Santa Barbara Basin, California). Applied and Environmental Microbiology 75:1487–1499.

27. Rossel PE, Elvert M, Ramette A, Boetius A, Hinrichs K-U. 2011. Factors controlling the distribution of anaerobic methanotrophic communities in marine environments: Evidence from intact polar membrane lipids. Geochimica et Cosmochimica Acta 75:164–184.

1070 28. Yanagawa K, Sunamura M, Lever MA, Morono Y, Hiruta A, Ishizaki O, Matsumoto R,
1071 Urabe T, Inagaki F. 2011. Niche Separation of Methanotrophic Archaea (ANME-1 and -2)
1072 in Methane-Seep Sediments of the Eastern Japan Sea Offshore Joetsu. Geomicrobiology
1073 Journal 28:118–129.

1074 29. Chen Y, Xu C, Wu N, Sun Z, Liu C, Zhen Y, Xin Y, Zhang X, Geng W, Cao H, Zhai B,
1075 Li J, Qin S, Zhou Y. 2022. Diversity of Anaerobic Methane Oxidizers in the Cold Seep
1076 Sediments of the Okinawa Trough. Front Microbiol 13.

1077 30. Cui H, Su X, Chen F, Holland M, Yang S, Liang J, Su P, Dong H, Hou W. 2019.
1078 Microbial diversity of two cold seep systems in gas hydrate-bearing sediments in the
1079 South China Sea. Marine Environmental Research 144:230–239.

1080 31. Chen J, Li Y, Zhong C, Xu Z, Lu G, Jing H, Liu H. 2023. Genomic Insights into Niche
1081 Partitioning across Sediment Depth among Anaerobic Methane-Oxidizing Archaea in
1082 Global Methane Seeps. mSystems 8:e01179-22.

1083 32. Zhang C, Fang Y-X, Yin X, Lai H, Kuang Z, Zhang T, Xu X-P, Wegener G, Wang J-H,
1084 Dong X. 2023. The majority of microorganisms in gas hydrate-bearing subseafloor
1085 sediments ferment macromolecules. Microbiome 11:37.

1086 33. Paull CK, Normark WR, Ussler W, Caress DW, Keaten R. 2008. Association among
1087 active seafloor deformation, mound formation, and gas hydrate growth and accumulation
1088 within the seafloor of the Santa Monica Basin, offshore California. Marine Geology
1089 250:258–275.

34. Normark WR, Piper DJW, Sliter R. 2006. Sea-level and tectonic control of middle to late Pleistocene turbidite systems in Santa Monica Basin, offshore California. Sedimentology 53:867–897.

35. Althoff PL. 1977. Structural refinements of dolomite and a magnesian calcite and implications for dolomite formation in the marine environment. American Mineralogist 62:772–783.

36. Ussler W, Paull CK. 2008. Rates of anaerobic oxidation of methane and authigenic carbonate mineralization in methane-rich deep-sea sediments inferred from models and geochemical profiles. Earth and Planetary Science Letters 266:271–287.

37. Komada T, Burdige DJ, Li H-L, Magen C, Chanton JP, Cada AK. 2016. Organic matter cycling across the sulfate-methane transition zone of the Santa Barbara Basin, California Borderland. Geochimica et Cosmochimica Acta 176:259–278.

38. Tarnovetskii IY, Merkel AY, Kanapatskiy TA, Ivanova EA, Gulin MB, Toshchakov S, Pimenov NV. 2018. Decoupling between sulfate reduction and the anaerobic oxidation of methane in the shallow methane seep of the Black sea. FEMS Microbiology Letters 365:fny235.

39. Kirkegaard RH, Dueholm MS, McIlroy SJ, Nierychlo M, Karst SM, Albertsen M, Nielsen PH. 2016. Genomic insights into members of the candidate phylum Hyd24-12 common in mesophilic anaerobic digesters. The ISME Journal 10:2352–2364.

1109 40. Schreiber L, Holler T, Knittel K, Meyerdierks A, Amann R. 2010. Identification of the
1110 dominant sulfate-reducing bacterial partner of anaerobic methanotrophs of the ANME-2
1111 clade. Environmental Microbiology 12:2327–2340.

1112 41. McGlynn SE, Chadwick GL, Kempes CP, Orphan VJ. 2015. Single cell activity reveals
1113 direct electron transfer in methanotrophic consortia. Nature 526:531–535.

1114 42. Metcalfe KS, Murali R, Mullin SW, Connon SA, Orphan VJ. 2021. Experimentally-
1115 validated correlation analysis reveals new anaerobic methane oxidation partnerships with
1116 consortium-level heterogeneity in diazotrophy. ISME J 15:377–396.

1117 43. Murali R, Yu H, Speth DR, Wu F, Metcalfe KS, Crémière A, Laso-Pèrez R, Malmstrom
1118 RR, Goudeau D, Woyke T, Hatzenpichler R, Chadwick GL, Connon SA, Orphan VJ.
1119 2023. Physiological potential and evolutionary trajectories of syntrophic sulfate-reducing
1120 bacterial partners of anaerobic methanotrophic archaea. PLOS Biology 21:e3002292.

1121 44. Nobu MK, Narihiro T, Kuroda K, Mei R, Liu W-T. 2016. Chasing the elusive
1122 Euryarchaeota class WSA2: genomes reveal a uniquely fastidious methyl-reducing
1123 methanogen. 10. ISME J 10:2478–2487.

1124 45. Dhillon A, Lever M, Lloyd KG, Albert DB, Sogin ML, Teske A. 2005. Methanogen
1125 Diversity Evidenced by Molecular Characterization of Methyl Coenzyme M Reductase A
1126 (mcrA) Genes in Hydrothermal Sediments of the Guaymas Basin. Applied and
1127 Environmental Microbiology 71:4592–4601.

1128 46. Teske A, Wegener G, Chanton JP, White D, MacGregor B, Hoer D, de Beer D, Zhuang G,
1129 Saxton MA, Joye SB, Lizarralde D, Soule SA, Ruff SE. 2021. Microbial Communities

1130 Under Distinct Thermal and Geochemical Regimes in Axial and Off-Axis Sediments of
1131 Guaymas Basin. Frontiers in Microbiology 12.

1132 47. Lai H, Deng Y, Yang L, Liang J, Dai L, Li L, Fang Y, Liu L, Kuang Z. 2023. Origin of
1133 natural gas within the deep-sea uncompacted sediments of the Shenhu area, northern
1134 South China Sea: Geochemical and methanogenic cultivation results. Marine and
1135 Petroleum Geology 147:106015.

1136 48. Coon GR, Duesing PD, Paul R, Baily JA, Lloyd KG. 2023. Biological methane production
1137 and accumulation under sulfate-rich conditions at Cape Lookout Bight, NC. Front
1138 Microbiol 14.

1139 49. Hatzenpichler R, Connon SA, Goudeau D, Malmstrom RR, Woyke T, Orphan VJ. 2016.
1140 Visualizing in situ translational activity for identifying and sorting slow-growing
1141 archaeal−bacterial consortia. PNAS 113:E4069–E4078.

1142 50. Krukenberg V, Riedel D, Gruber-Vodicka HR, Buttigieg PL, Tegetmeyer HE, Boetius A,
1143 Wegener G. 2018. Gene expression and ultrastructure of meso- and thermophilic
1144 methanotrophic consortia. Environmental Microbiology 20:1651–1666.

1145 51. Hatzenpichler R, Scheller S, Tavormina PL, Babin BM, Tirrell DA, Orphan VJ. 2014. In
1146 situ visualization of newly synthesized proteins in environmental microbes using amino
1147 acid tagging and click chemistry. Environmental Microbiology 16:2568–2590.

1148 52. Hatzenpichler R, Orphan VJ. 2016. Detection of Protein-Synthesizing Microorganisms in
1149 the Environment via Bioorthogonal Noncanonical Amino Acid Tagging (BONCAT), p.
1150 145–157. *In* McGenity, TJ, Timmis, KN, Nogales, B (eds.), Hydrocarbon and Lipid

Microbiology Protocols: Single-Cell and Single-Molecule Methods. Springer, Berlin, Heidelberg.

53. Schmale O, Leifer I, Deimling JS v., Stolle C, Krause S, Kießlich K, Frahm A, Treude T. 2015. Bubble Transport Mechanism: Indications for a gas bubble-mediated inoculation of benthic methanotrophs into the water column. Continental Shelf Research 103:70–78.

54. Crémière A, Lepland A, Chand S, Sahy D, Kirsimäe K, Bau M, Whitehouse MJ, Noble SR, Martma T, Thorsnes T, Brunstad H. 2016. Fluid source and methane-related diagenetic processes recorded in cold seep carbonates from the Alvheim channel, central North Sea. Chemical Geology 432:16–33.

55. Tryon MD, Brown KM, Torres ME. 2002. Fluid and chemical flux in and out of sediments hosting methane hydrate deposits on Hydrate Ridge, OR, II: Hydrological processes. Earth and Planetary Science Letters 201:541–557.

56. Treude T, Boetius A, Knittel K, Wallmann K, Barker Jørgensen B. 2003. Anaerobic oxidation of methane above gas hydrates at Hydrate Ridge, NE Pacific Ocean. Mar Ecol Prog Ser 264:1–14.

57. Heeschen KU, Collier RW, de Angelis MA, Suess E, Rehder G, Linke P, Klinkhammer GP. 2005. Methane sources, distributions, and fluxes from cold vent sites at Hydrate Ridge, Cascadia Margin. Global Biogeochemical Cycles 19.

58. Stadnitskaia A, Muyzer G, Abbas B, Coolen MJL, Hopmans EC, Baas M, van Weering TCE, Ivanov MK, Poludetkina E, Sinninghe Damsté JS. 2005. Biomarker and 16S rDNA

evidence for anaerobic oxidation of methane and related carbonate precipitation in deep-sea mud volcanoes of the Sorokin Trough, Black Sea. Marine Geology 217:67–96.

59. Stadnitskaia A, Nadezhkin D, Abbas B, Blinova V, Ivanov MK, Sinninghe Damsté JS. 2008. Carbonate formation by anaerobic oxidation of methane: Evidence from lipid biomarker and fossil 16S rDNA. Geochimica et Cosmochimica Acta 72:1824–1836.

60. Lloyd KG, Albert DB, Biddle JF, Chanton JP, Pizarro O, Teske A. 2010. Spatial Structure and Activity of Sedimentary Microbial Communities Underlying a Beggiatoa spp. Mat in a Gulf of Mexico Hydrocarbon Seep. PLOS ONE 5:e8738.

61. Meister P, Liu B, Khalili A, Böttcher ME, Jørgensen BB. 2019. Factors controlling the carbon isotope composition of dissolved inorganic carbon and methane in marine porewater: An evaluation by reaction-transport modelling. Journal of Marine Systems 200:103227.

62. Peckmann J, Reimer A, Luth U, Luth C, Hansen BT, Heinicke C, Hoefs J, Reitner J. 2001. Methane-derived carbonates and authigenic pyrite from the northwestern Black Sea. Marine Geology 177:129–150.

63. Magalhães VH, Pinheiro LM, Ivanov MK, Kozlova E, Blinova V, Kolganova J, Vasconcelos C, McKenzie JA, Bernasconi SM, Kopf AJ, Díaz-del-Río V, González FJ, Somoza L. 2012. Formation processes of methane-derived authigenic carbonates from the Gulf of Cadiz. Sedimentary Geology 243–244:155–168.

64. Greinert J, Bohrmann G, Suess E. 2001. Gas Hydrate-Associated Carbonates and Methane-Venting at Hydrate Ridge: Classification, Distribution, and Origin of Authigenic

Lithologies, p. 99–113. *In* Natural Gas Hydrates: Occurrence, Distribution, and Detection. American Geophysical Union (AGU).

65. Aloisi G, Bouloubassi I, Heijs SK, Pancost RD, Pierre C, Sinninghe Damsté JS, Gottschal JC, Forney LJ, Rouchy J-M. 2002. CH4-consuming microorganisms and the formation of carbonate crusts at cold seeps. Earth and Planetary Science Letters 203:195–203.

66. Knittel K, Lösekann T, Boetius A, Kort R, Amann R. 2005. Diversity and Distribution of Methanotrophic Archaea at Cold Seeps. Applied and Environmental Microbiology 71:467–479.

67. Orcutt B, Boetius A, Elvert M, Samarkin V, Joye SB. 2005. Molecular biogeochemistry of sulfate reduction, methanogenesis and the anaerobic oxidation of methane at Gulf of Mexico cold seeps. Geochimica et Cosmochimica Acta 69:4267–4281.

68. Treude T, Knittel K, Blumenberg M, Seifert R, Boetius A. 2005. Subsurface Microbial Methanotrophic Mats in the Black Sea. Applied and Environmental Microbiology 71:6375–6378.

69. Treude T, Orphan V, Knittel K, Gieseke A, House CH, Boetius A. 2007. Consumption of Methane and CO2 by Methanotrophic Microbial Mats from Gas Seeps of the Anoxic Black Sea. Applied and Environmental Microbiology 73:2271–2283.

70. House CH, Orphan VJ, Turk KA, Thomas B, Pernthaler A, Vrentas JM, Joye SB. 2009. Extensive carbon isotopic heterogeneity among methane seep microbiota. Environmental Microbiology 11:2207–2215.

1212 71. Ruff SE, Kuhfuss H, Wegener G, Lott C, Ramette A, Wiedling J, Knittel K, Weber M.
1213 2016. Methane Seep in Shallow-Water Permeable Sediment Harbors High Diversity of
1214 Anaerobic Methanotrophic Communities, Elba, Italy. Frontiers in Microbiology 7.

1215 72. Webster G, Parkes RJ, Fry JC, Weightman AJ. 2004. Widespread Occurrence of a Novel
1216 Division of Bacteria Identified by 16S rRNA Gene Sequences Originally Found in Deep
1217 Marine Sediments. Applied and Environmental Microbiology 70:5708–5713.

1218 73. Lee YM, Hwang K, Lee JI, Kim M, Hwang CY, Noh H-J, Choi H, Lee HK, Chun J, Hong
1219 SG, Shin SC. 2018. Genomic Insight Into the Predominance of Candidate Phylum
1220 Atribacteria JS1 Lineage in Marine Sediments. Front Microbiol 9.

1221 74. Chakraborty A, Ruff SE, Dong X, Ellefson ED, Li C, Brooks JM, McBee J, Bernard BB,
1222 Hubert CRJ. 2020. Hydrocarbon seepage in the deep seabed links subsurface and seafloor
1223 biospheres. PNAS 117:11029–11037.

1224 75. Liu Y-F, Qi Z-Z, Shou L-B, Liu J-F, Yang S-Z, Gu J-D, Mu B-Z. 2019. Anaerobic
1225 hydrocarbon degradation in candidate phylum 'Atribacteria' (JS1) inferred from
1226 genomics. The ISME Journal 13:2377–2390.

1227 76. Biddle JF, Cardman Z, Mendlovitz H, Albert DB, Lloyd KG, Boetius A, Teske A. 2012.
1228 Anaerobic oxidation of methane at different temperature regimes in Guaymas Basin
1229 hydrothermal sediments. ISME J 6:1018–1031.

1230 77. Bertram S, Blumenberg M, Michaelis W, Siegert M, Krüger M, Seifert R. 2013.
1231 Methanogenic capabilities of ANME-archaea deduced from -labelling approaches.
1232 Environmental Microbiology 15:2384–2393.

78. Beulig F, Røy H, McGlynn SE, Jørgensen BB. 2019. Cryptic CH4 cycling in the sulfate–methane transition of marine sediments apparently mediated by ANME-1 archaea. The ISME Journal 13:250–262.

79. Kevorkian RT, Callahan S, Winstead R, Lloyd KG. 2021. ANME-1 archaea may drive methane accumulation and removal in estuarine sediments. Environ Microbiol Rep 13:185–194.

80. Chadwick GL, Skennerton CT, Laso-Pérez R, Leu AO, Speth DR, Yu H, Morgan-Lang C, Hatzenpichler R, Goudeau D, Malmstrom R, Brazelton WJ, Woyke T, Hallam SJ, Tyson GW, Wegener G, Boetius A, Orphan VJ. 2022. Comparative genomics reveals electron transfer and syntrophic mechanisms differentiating methanotrophic and methanogenic archaea. PLOS Biology 20:e3001508.

81. Conrad R. 2005. Quantification of methanogenic pathways using stable carbon isotopic signatures: a review and a proposal. Organic Geochemistry 36:739–752.

82. Chatterjee S, Dickens GR, Bhatnagar G, Chapman WG, Dugan B, Snyder GT, Hirasaki GJ. 2011. Pore water sulfate, alkalinity, and carbon isotope profiles in shallow sediment above marine gas hydrate systems: A numerical modeling perspective. Journal of Geophysical Research: Solid Earth 116.

83. Beal EJ, House CH, Orphan VJ. 2009. Manganese- and Iron-Dependent Marine Methane Oxidation. Science 325:184–187.

84. Riedinger N, Formolo MJ, Lyons TW, Henkel S, Beck A, Kasten S. 2014. An inorganic geochemical argument for coupled anaerobic oxidation of methane and iron reduction in marine sediments. Geobiology 12:172–181.

85. Oni OE, Miyatake T, Kasten S, Richter-Heitmann T, Fischer D, Wagenknecht L, Ksenofontov V, Kulkarni A, Blumers M, Shylin S, Costa B, Klingelhöfer G, Friedrich MW. 2015. Distinct microbial populations are tightly linked to the profile of dissolved iron in the methanic sediments of the Helgoland mud area, North Sea. Front Microbiol 6.

86. Sun Z, Wei H, Zhang X, Shang L, Yin X, Sun Y, Xu L, Huang W, Zhang X. 2015. A unique Fe-rich carbonate chimney associated with cold seeps in the Northern Okinawa Trough, East China Sea. Deep Sea Research Part I: Oceanographic Research Papers 95:37–53.

87. Egger M, Rasigraf O, Sapart CJ, Jilbert T, Jetten MSM, Röckmann T, van der Veen C, Bândă N, Kartal B, Ettwig KF, Slomp CP. 2015. Iron-Mediated Anaerobic Oxidation of Methane in Brackish Coastal Sediments. Environ Sci Technol 49:277–283.

88. Egger M, Hagens M, Sapart CJ, Dijkstra N, van Helmond NAGM, Mogollón JM, Risgaard-Petersen N, van der Veen C, Kasten S, Riedinger N, Böttcher ME, Röckmann T, Jørgensen BB, Slomp CP. 2017. Iron oxide reduction in methane-rich deep Baltic Sea sediments. Geochimica et Cosmochimica Acta 207:256–276.

89. Rooze J, Egger M, Tsandev I, Slomp CP. 2016. Iron-dependent anaerobic oxidation of methane in coastal surface sediments: Potential controls and impact. Limnology and Oceanography 61:S267–S282.

1273 90. Li J, Peng X, Bai S, Chen Z, Van Nostrand JD. 2018. Biogeochemical processes
1274 controlling authigenic carbonate formation within the sediment column from the Okinawa
1275 Trough. Geochimica et Cosmochimica Acta 222:363–382.

1276 91. Aromokeye DA, Kulkarni AC, Elvert M, Wegener G, Henkel S, Coffinet S, Eickhorst T,
1277 Oni OE, Richter-Heitmann T, Schnakenberg A, Taubner H, Wunder L, Yin X, Zhu Q,
1278 Hinrichs K-U, Kasten S, Friedrich MW. 2020. Rates and Microbial Players of Iron-Driven
1279 Anaerobic Oxidation of Methane in Methanic Marine Sediments. Front Microbiol 10.

1280 92. Mitterer RM. 2010. Methanogenesis and sulfate reduction in marine sediments: A new
1281 model. Earth and Planetary Science Letters 295:358–366.

1282 93. Dell'Anno A, Stefano B, Danovaro R. 2002. Quantification, base composition, and fate of
1283 extracellular DNA in marine sediments. Limnology and Oceanography 47:899–905.

1284 94. Dell'Anno A, Danovaro R. 2005. Extracellular DNA Plays a Key Role in Deep-Sea
1285 Ecosystem Functioning. Science 309:2179–2179.

1286 95. Torti A, Lever MA, Jørgensen BB. 2015. Origin, dynamics, and implications of
1287 extracellular DNA pools in marine sediments. Marine Genomics 24:185–196.

1288 96. Lennon JT, Muscarella ME, Placella SA, Lehmkuhl BK. 2018. How, When, and Where
1289 Relic DNA Affects Microbial Diversity. mBio 9:10.1128/mbio.00637-18.

1290 97. Torti A, Jørgensen BB, Lever MA. 2018. Preservation of microbial DNA in marine
1291 sediments: insights from extracellular DNA pools. Environmental Microbiology 20:4526–
1292 4542.

1293 98. Cai W-J, Chen F, Powell EN, Walker SE, Parsons-Hubbard KM, Staff GM, Wang Y,
1294 Ashton-Alcox KA, Callender WR, Brett CE. 2006. Preferential dissolution of carbonate
1295 shells driven by petroleum seep activity in the Gulf of Mexico. Earth and Planetary
1296 Science Letters 248:227–243.

1297 99. Himmler T, Brinkmann F, Bohrmann G, Peckmann J. 2011. Corrosion patterns of seep-
1298 carbonates from the eastern Mediterranean Sea. Terra Nova 23:206–212.

1299 100. Matsumoto R. 1990. Vuggy carbonate crust formed by hydrocarbon seepage on the
1300 continental shelf of Baffin Island, northeast Canada. Geochemical Journal 24:143–158.

1301 101. Carson B, Kastner M, Bartlett D, Jaeger J, Jannasch H, Weinstein Y. 2003. Implications of
1302 carbon flux from the Cascadia accretionary prism: results from long-term, in situ
1303 measurements at ODP Site 892B. Marine Geology 198:159–180.

1304 102. Krause S, Aloisi G, Engel A, Liebetrau V, Treude T. 2014. Enhanced Calcite Dissolution
1305 in the Presence of the Aerobic Methanotroph Methylosinus trichosporium.
1306 Geomicrobiology Journal 31:325–337.

1307 103. Leprich DJ, Flood BE, Schroedl PR, Ricci E, Marlow JJ, Girguis PR, Bailey JV. 2021.
1308 Sulfur bacteria promote dissolution of authigenic carbonates at marine methane seeps.
1309 ISME J 15:2043–2056.

1310 104. Dulbecco R, Vogt M. 1954. PLAQUE FORMATION AND ISOLATION OF PURE
1311 LINES WITH POLIOMYELITIS VIRUSES. Journal of Experimental Medicine 99:167–
1312 182.

105. Reeburgh WS. 1967. An Improved Interstitial Water Sampler. Limnology and Oceanography 12:163–165.

106. Cline JD. 1969. Spectrophotometric Determination of Hydrogen Sulfide in Natural Waters. Limnology and Oceanography 14:454–458.

107. Coplen TB, Brand WA, Gehre M, Gröning M, Meijer HAJ, Toman B, Verkouteren RM. 2006. New Guidelines for δ13C Measurements. Anal Chem 78:2439–2441.

108. Standard Test Methods for Density and Specific Gravity (Relative Density) of Plastics by Displacement. https://www.astm.org/d0792-20.html. Retrieved 19 September 2024.

109. Giesche H. 2006. Mercury Porosimetry: A General (Practical) Overview. Particle & Particle Systems Characterization 23:9–19.

110. Kozich JJ, Westcott SL, Baxter NT, Highlander SK, Schloss PD. 2013. Development of a Dual-Index Sequencing Strategy and Curation Pipeline for Analyzing Amplicon Sequence Data on the MiSeq Illumina Sequencing Platform. Appl Environ Microbiol 79:5112–5120.

111. Martin M. 2011. Cutadapt removes adapter sequences from high-throughput sequencing reads. 1. EMBnet.journal 17:10–12.

112. Bolyen E, Rideout JR, Dillon MR, Bokulich NA, Abnet CC, Al-Ghalith GA, Alexander H, Alm EJ, Arumugam M, Asnicar F, Bai Y, Bisanz JE, Bittinger K, Brejnrod A, Brislawn CJ, Brown CT, Callahan BJ, Caraballo-Rodríguez AM, Chase J, Cope EK, Da Silva R, Diener C, Dorrestein PC, Douglas GM, Durall DM, Duvallet C, Edwardson CF, Ernst M, Estaki M, Fouquier J, Gauglitz JM, Gibbons SM, Gibson DL, Gonzalez A, Gorlick K,

1333 Guo J, Hillmann B, Holmes S, Holste H, Huttenhower C, Huttley GA, Janssen S,
1334 Jarmusch AK, Jiang L, Kaehler BD, Kang KB, Keefe CR, Keim P, Kelley ST, Knights D,
1335 Koester I, Kosciolek T, Kreps J, Langille MGI, Lee J, Ley R, Liu Y-X, Loftfield E,
1336 Lozupone C, Maher M, Marotz C, Martin BD, McDonald D, McIver LJ, Melnik AV,
1337 Metcalf JL, Morgan SC, Morton JT, Naimey AT, Navas-Molina JA, Nothias LF,
1338 Orchanian SB, Pearson T, Peoples SL, Petras D, Preuss ML, Pruesse E, Rasmussen LB,
1339 Rivers A, Robeson MS, Rosenthal P, Segata N, Shaffer M, Shiffer A, Sinha R, Song SJ,
1340 Spear JR, Swafford AD, Thompson LR, Torres PJ, Trinh P, Tripathi A, Turnbaugh PJ, Ul-
1341 Hasan S, van der Hooft JJJ, Vargas F, Vázquez-Baeza Y, Vogtmann E, von Hippel M,
1342 Walters W, Wan Y, Wang M, Warren J, Weber KC, Williamson CHD, Willis AD, Xu ZZ,
1343 Zaneveld JR, Zhang Y, Zhu Q, Knight R, Caporaso JG. 2019. Reproducible, interactive,
1344 scalable and extensible microbiome data science using QIIME 2. Nat Biotechnol 37:852–
1345 857.

1346 113. Callahan BJ, McMurdie PJ, Rosen MJ, Han AW, Johnson AJA, Holmes SP. 2016.
1347 DADA2: High-resolution sample inference from Illumina amplicon data. Nature Methods
1348 13:581–583.

1349 114. Quast C, Pruesse E, Yilmaz P, Gerken J, Schweer T, Yarza P, Peplies J, Glöckner FO.
1350 2013. The SILVA ribosomal RNA gene database project: improved data processing and
1351 web-based tools. Nucleic Acids Research 41:D590–D596.

1352 115. Mayr MJ, Orphan VJ. 2024. Extraction of microbial cells from methane-seep carbonate
1353 rocks for single-cell analyses (e.g. BONCAT-FISH) using “combination buffer” and
1354 percoll density centrifugation https://doi.org/10.17504/protocols.io.rm7vzjk55lx1/v1.

1355 116. Eichorst SA, Strasser F, Woyke T, Schintlmeister A, Wagner M, Woebken D. 2015.
1356 Advancements in the application of NanoSIMS and Raman microspectroscopy to
1357 investigate the activity of microbial cells in soils. FEMS Microbiol Ecol 91:fiv106.

1358 117. Amann RI, Binder BJ, Olson RJ, Chisholm SW, Devereux R, Stahl DA. 1990.
1359 Combination of 16S rRNA-targeted oligonucleotide probes with flow cytometry for
1360 analyzing mixed microbial populations. Applied and Environmental Microbiology
1361 56:1919–1925.

1362 118. Daims H, Brühl A, Amann R, Schleifer K-H, Wagner M. 1999. The Domain-specific
1363 Probe EUB338 is Insufficient for the Detection of all *Bacteria*: Development and
1364 Evaluation of a more Comprehensive Probe Set. Systematic and Applied Microbiology
1365 22:434–444.

1366 119. Westram R, Bader K, Prüsse E, Kumar Y, Meier H, Glöckner FO, Ludwig W. 2011. ARB:
1367 A Software Environment for Sequence Data, p. 399–406. *In* Handbook of Molecular
1368 Microbial Ecology I. John Wiley & Sons, Ltd.

1369 120. Stahl DA, Amann R. 1991. Development and application of nucleic acid probes in bacterial
1370 systematics, p.205-248. *In* Stackebrandt, E. and Goodfellow, M., Eds., Nucleic Acid
1371 Techniques in Bacterial Systematics, John Wiley & Sons Ltd.

1372 121. Dieterich DC, Link AJ, Graumann J, Tirrell DA, Schuman EM. 2006. Selective
1373 identification of newly synthesized proteins in mammalian cells using bioorthogonal
1374 noncanonical amino acid tagging (BONCAT). Proceedings of the National Academy of
1375 Sciences 103:9482–9487.

1376 122. Sletten EM, Bertozzi CR. 2009. Bioorthogonal Chemistry: Fishing for Selectivity in a Sea
1377 of Functionality. Angewandte Chemie International Edition 48:6974–6998.

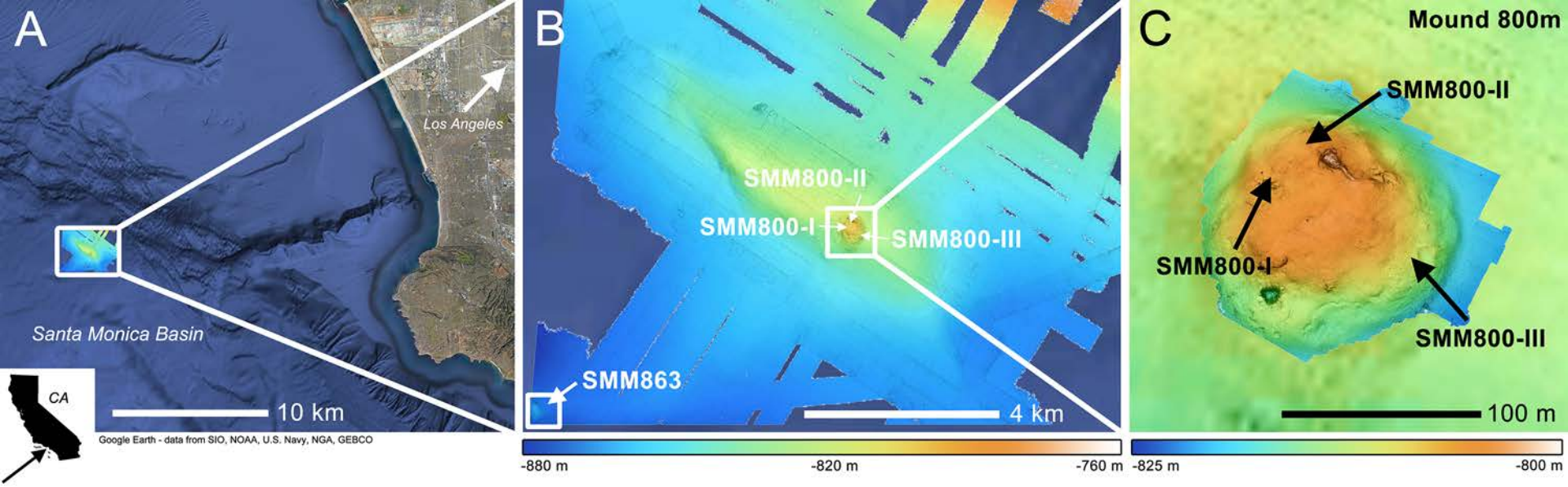


**Fig. 1** – A) General location of the Santa Monica Basin seep sites (NE Mound, 800m, and SW mound, 863m) sampled for this study; B) Multi-beam bathymetry map of the sampling seep areas at SMM 800 and SMM 863; C) higher-resolution bathymetry map of the seep areas sampled at SMM 800: SMM 800-I, SMM 800-II, and SMM 800-III. Bathymetry colors in B) and C) correspond to mapped depth. Bathymetry maps were collected by MBARI in 2018.

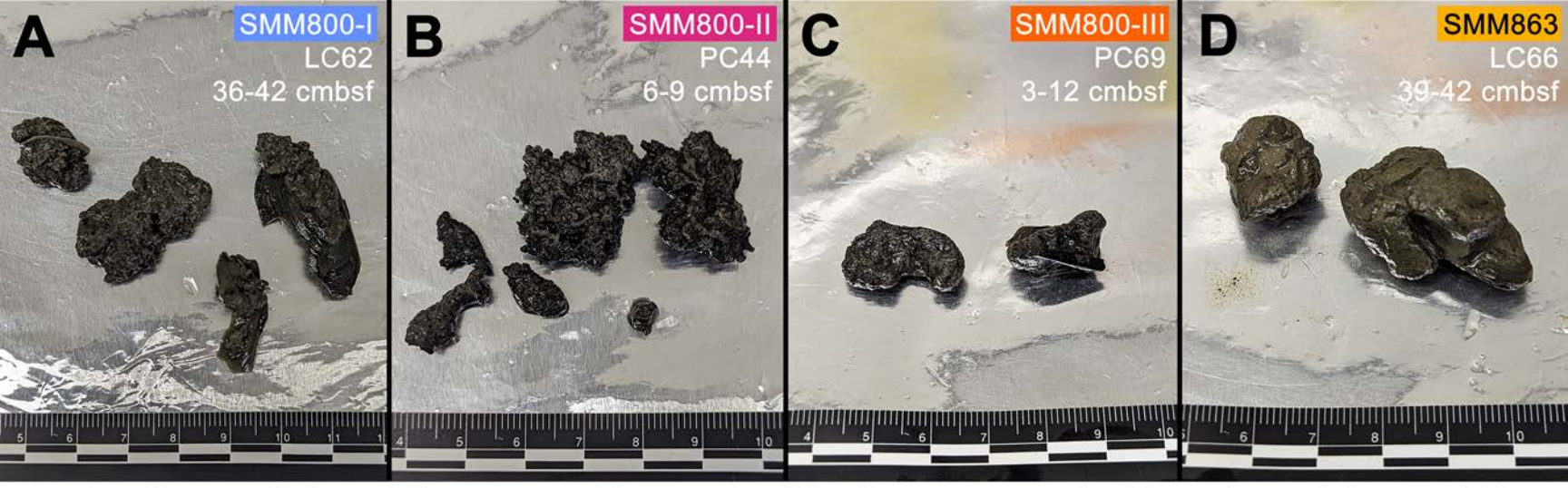


**Fig. 2** – Characteristic nodules recovered from each of the four seep areas in this study; Nodule morphology is remarkably consistent with depth (expressed as centimeters below seafloor, cmbsf); ruler markings are in cm; A) Nodules recovered from LC62's 36-42-cmbsf horizons at SMM 800-I; B) Nodules from PC44's 6-9-cmbsf horizon at SMM 800-II; C) Nodules recovered from PC69 (3-12-cmbsf) at SMM 800-III; D) Nodules recovered from the 39-42-cmbsf horizon of LC66 at SMM 863.

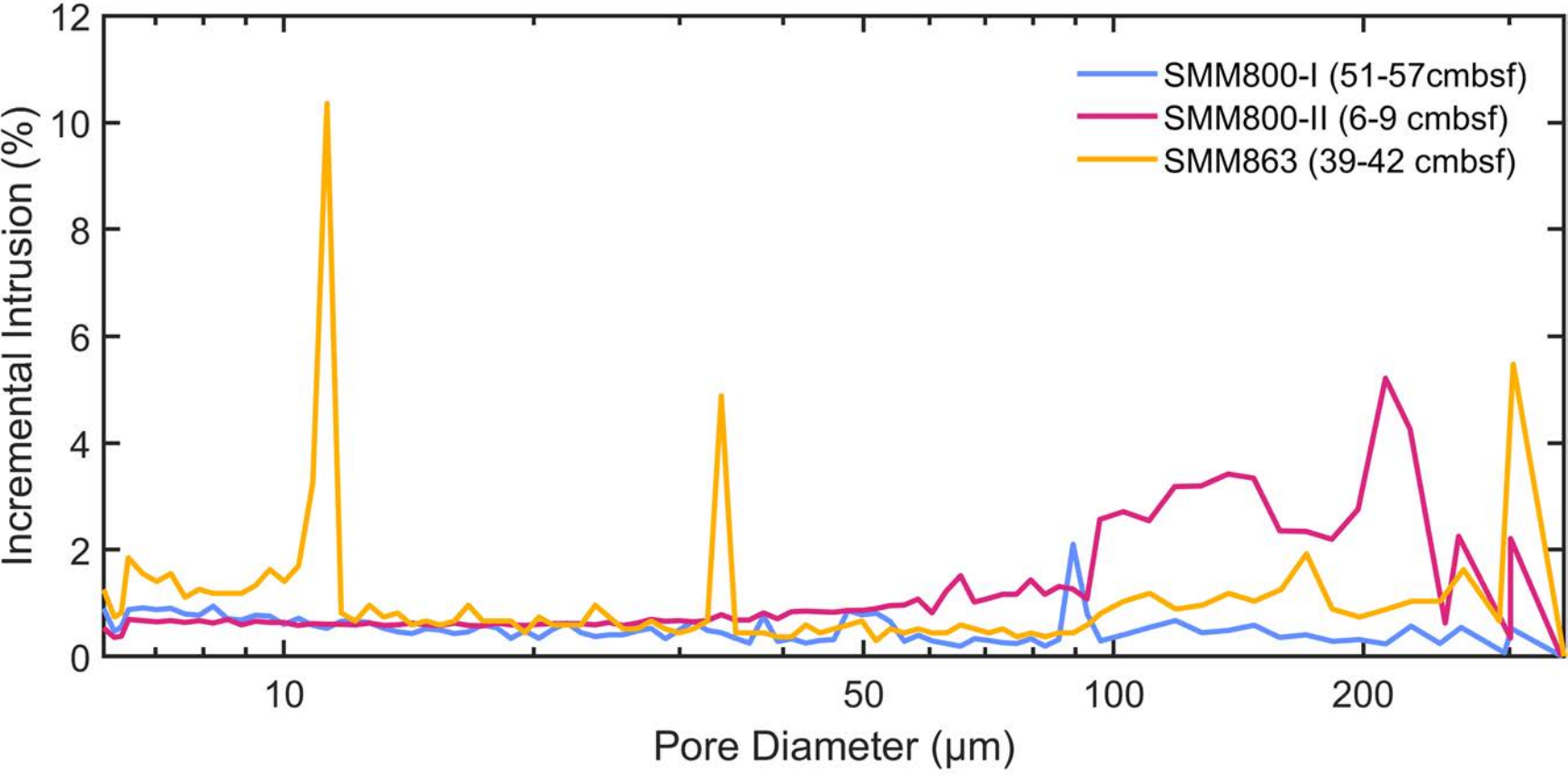


**Fig. 3** – Hg-porosimetry curves detailing pore diameter versus incremental intrusion for three nodules sampled from SMM 800-I, SMM 800-II, and SMM 863. Pore sizes observable with porosimetry range from 6- to 350-μm. The three nodules shed information on the three distinct nodule-featuring regions identified in this data set: 1) SMM 800 deep sediment (LC62), 2) SMM 800 shallow sediment (PC44), and 3) SMM 863 deep sediment (LC66)

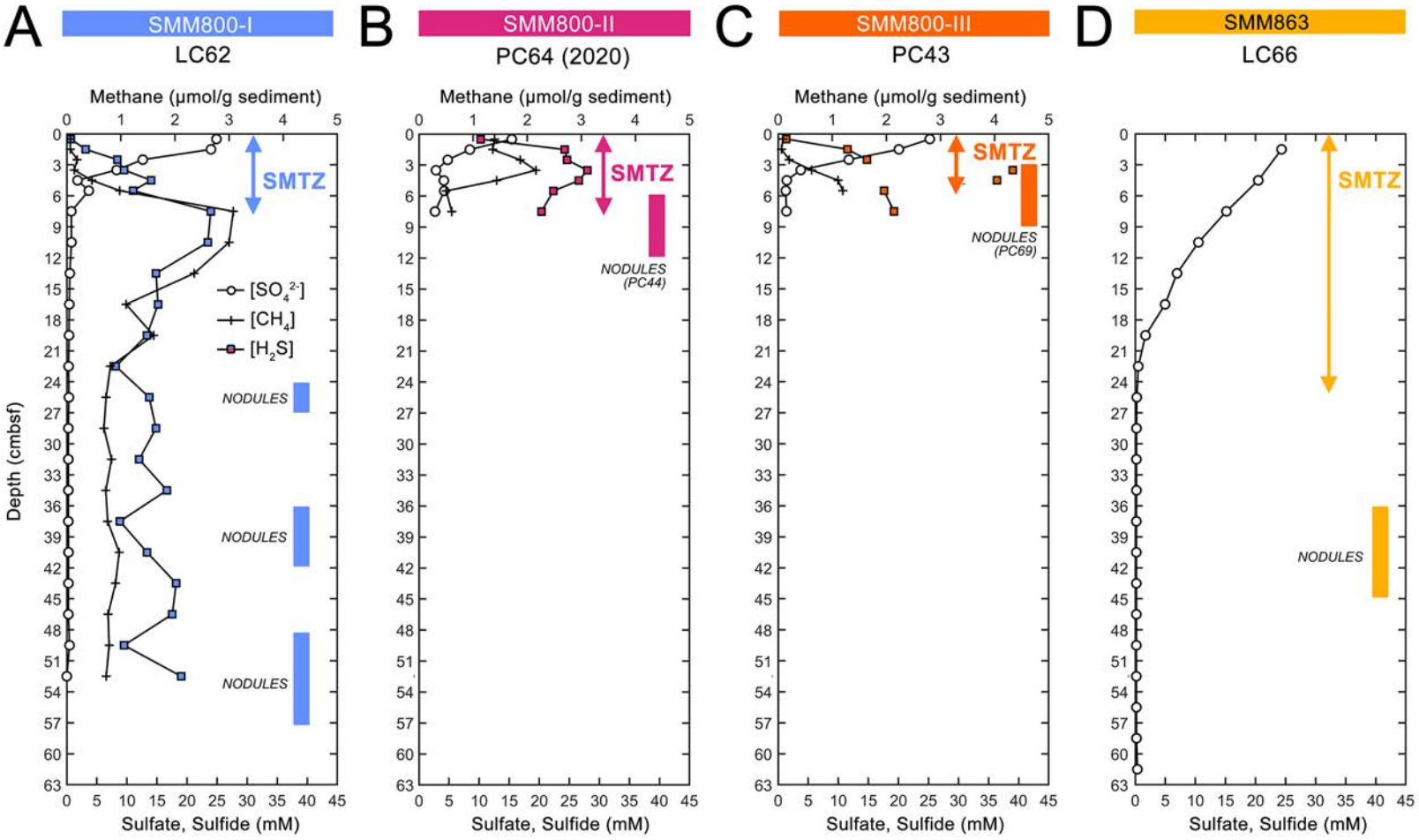


**Fig. 4** – Sulfate, methane, and sulfide concentration profiles collected for sediment porewaters at the seep areas investigated in this study. We plot the median depth in centimeters below seafloor (cmbsf), where concentrations represent 3-cm depth horizons. The sulfate-methane transition zones (SMTZ), as determined by near-complete(<<1mM) sulfate drawdown in each core, are also demonstrated with colored arrows. Colored bars represent the horizons where nodules were recovered for further analysis. Nodules recovered from a different, co-located core at the seep area are also specified. PC64 from SMM 800-II was collected a year previously. We note that there are greater uncertainties with measured sulfide concentrations above the detection limit (>25mM, e.g., in PC43 from SMM 800-III). Only sulfate porewater concentration was collected for the core at SMM 863.

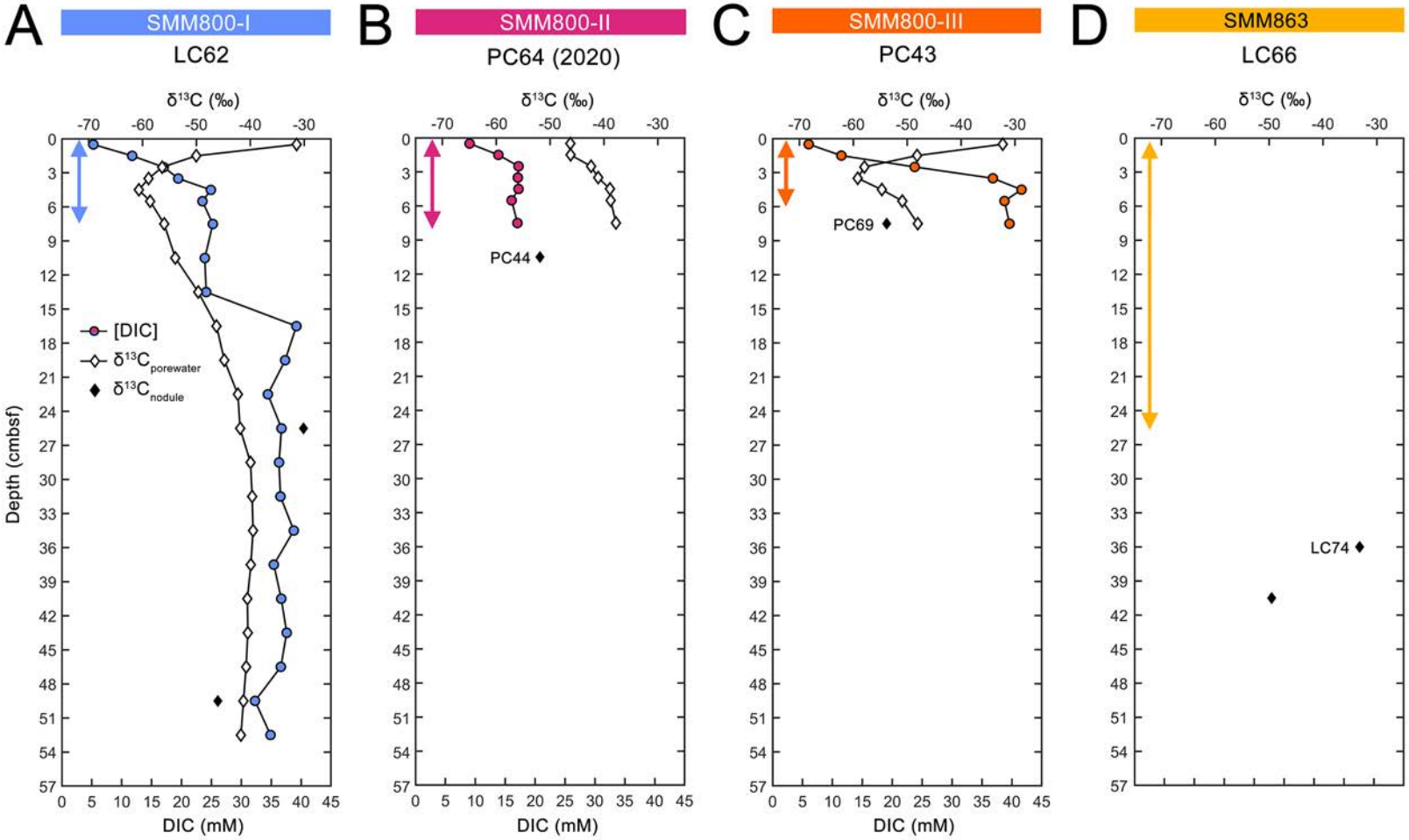


**Fig. 5** – Sediment porewater DIC, $\delta^{13}C_{porewater}$, and $\delta^{13}C_{nodule}$ profiles collected at the seep areas investigated in this study. We plot the median depth in centimeters below seafloor (cmbsf), where values represent multiple depth horizons. Because of the <3‰ spread between $\delta^{13}C_{nodule}$ replicates, values are simply averaged for comparison (individual values are included in Table S2). Colored arrows indicate an estimate for the location of the SMTZ, as in Fig. 4. PC64 from SMM 800-II was collected a year previously. Only $\delta^{13}C_{nodule}$ was able to be collected for the cores at SMM 863.

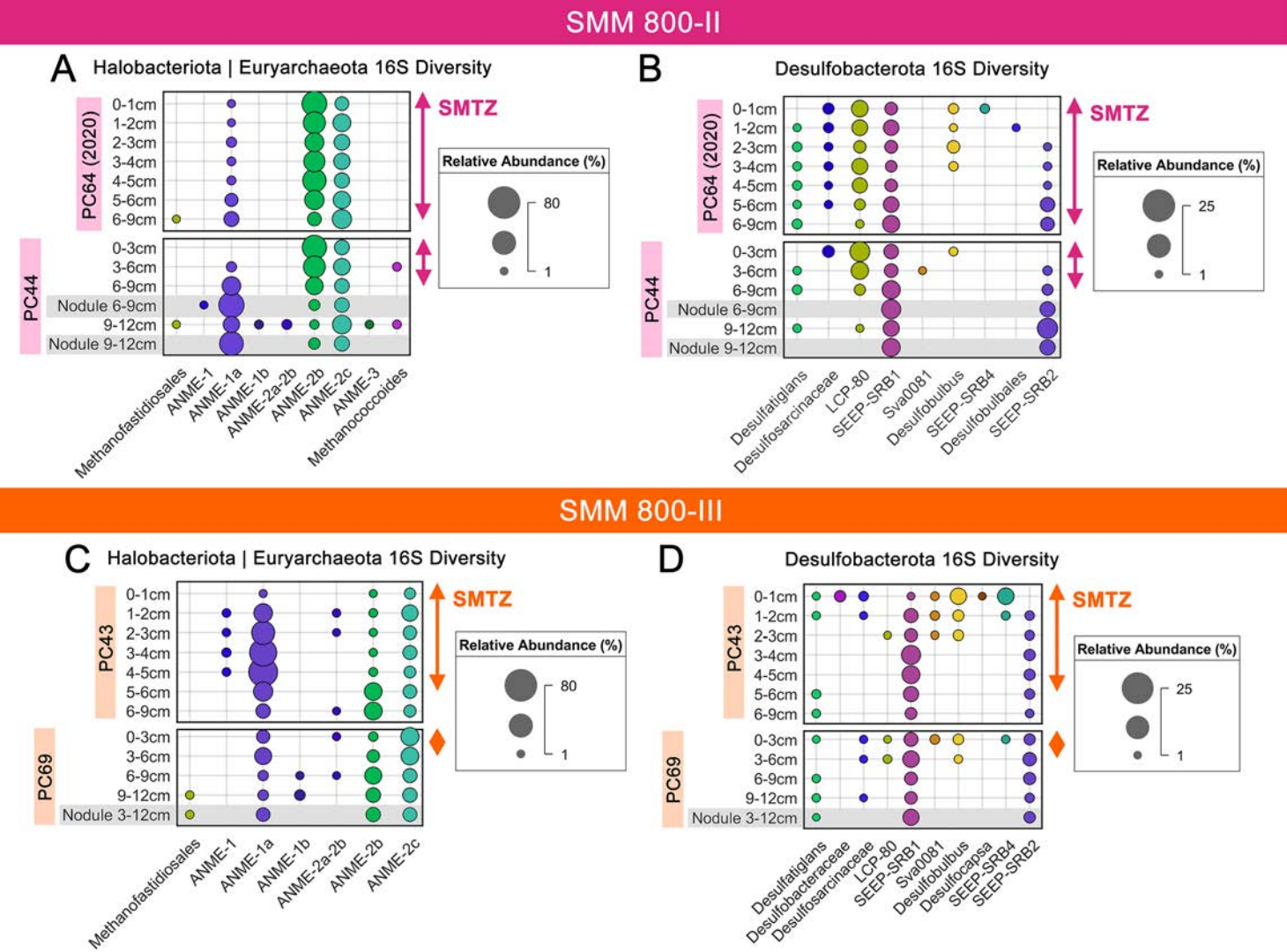


**Fig. 6** – Bubble plots summarizing the depth-resolved, 16S relative abundances for groups within *Halobacteriota* (featuring ANME), *Euryarchaeota* (featuring methanogens, e.g., *Methanofastidiosales*), and *Desulfobacterota* (featuring sulfate-reducing partners to ANME) in PC64 and PC44 at SMM 800-II (A, B), as well as PC43 and PC69 at SMM 800-III (C, D) . Where possible, ASVs within these phyla were grouped at the genus-level, or at the next highest taxonomic level possible, and then cut off below a minimum 1% relative abundance. Communities extracted from nodules are highlighted in grey and often represent larger depth horizons. The location of the sulfate-methane transition zone (SMTZ) according to porewater sulfate concentrations from the same or co-located sediment core is indicated with the colored arrows.

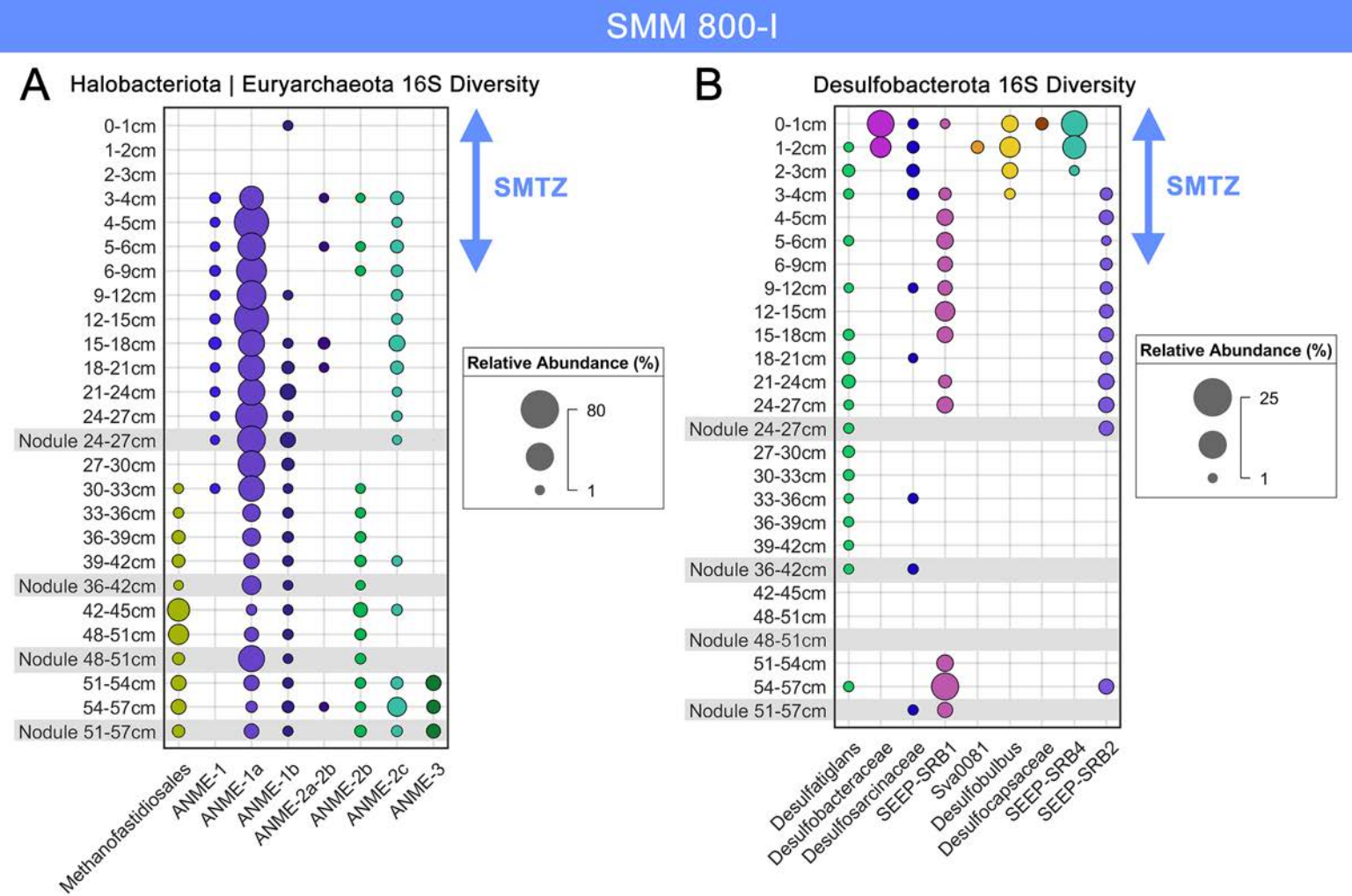


**Fig. 7** – Bubble plots summarizing the depth-resolved, 16S relative abundances for groups within *Halobacteriota*, *Euryarchaeota*, and *Desulfobacterota* in LC62 at SMM 800-I. Where possible, ASVs within these phyla were grouped at the genus-level, or at the next highest taxonomic level possible, and then cut off below a minimum 1% relative abundance. Communities extracted from nodules are highlighted in grey and often represent larger depth horizons. The location of the sulfate-methane transition zone (SMTZ) according to porewater sulfate concentrations from the same or co-located sediment core is indicated with the colored arrows. A) Relative abundances within prominent phyla *Halobacteriota* (featuring ANME) and *Euryarchaeota* (featuring methanogens such as *Methanofastidiosales*). B) Relative abundances within *Desulfobacterota* – the phylum with sulfate-reducing partners to ANME.

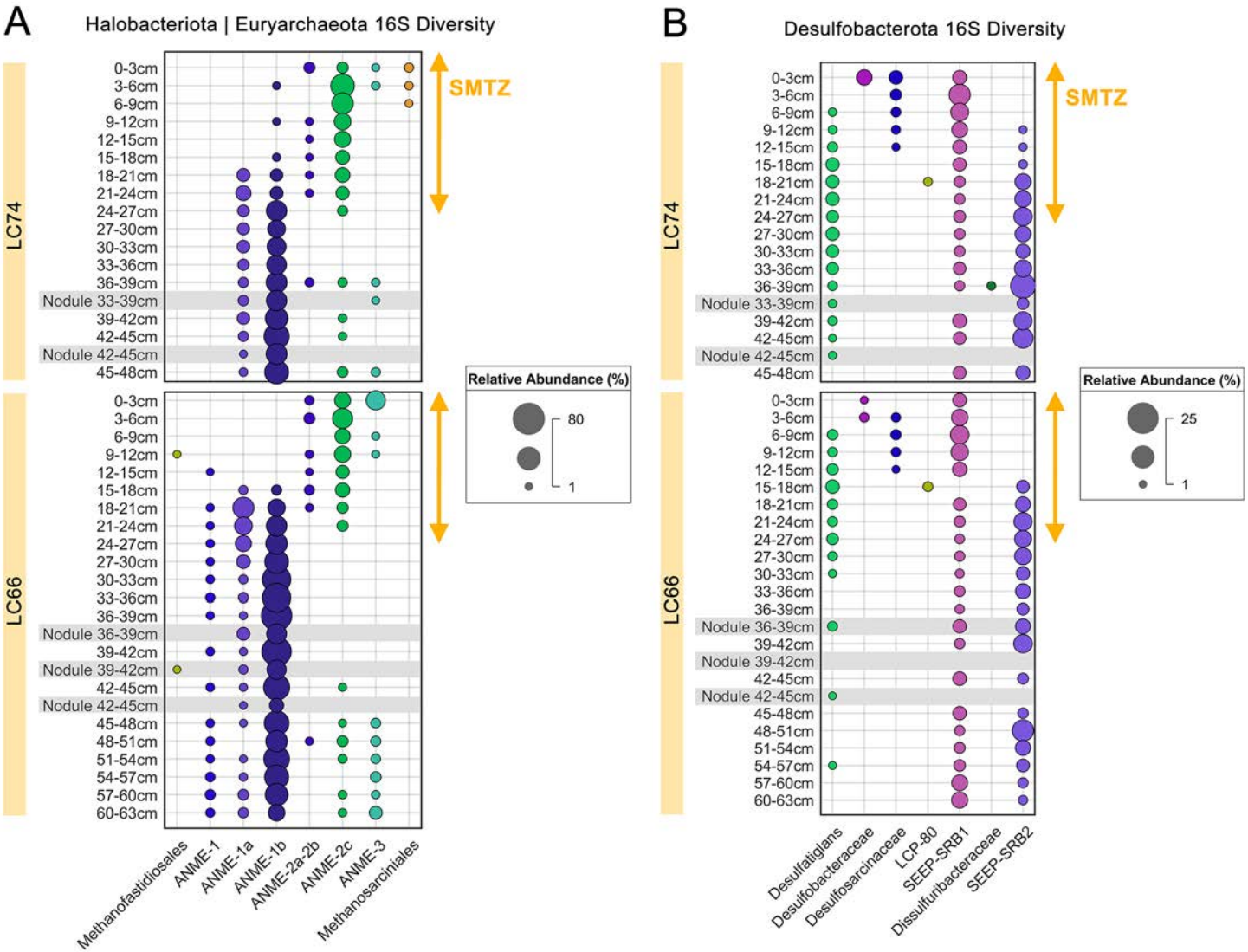


**Fig. 8** – Bubble plots summarizing the depth-resolved, 16S relative abundances for groups within *Halobacteriota*, *Euryarchaeota*, and *Desulfobacterota* in LC74 and LC66 at SMM 863. Where possible, ASVs within these phyla were grouped at the genus-level, or at the next highest taxonomic level possible, and then cut off below a minimum 1% relative abundance. Communities extracted from nodules are highlighted in grey and often represent larger depth horizons. The location of the sulfate-methane transition zone (SMTZ) according to porewater sulfate concentrations from the same or co-located sediment core is indicated with the colored arrows. A) Relative abundances within prominent phyla *Halobacteriota* (featuring ANME) and *Euryarchaeota* (featuring methanogens such as *Methanofastidiosales*). B) Relative abundances within *Desulfobacterota* – the phylum with sulfate-reducing partners to ANME.

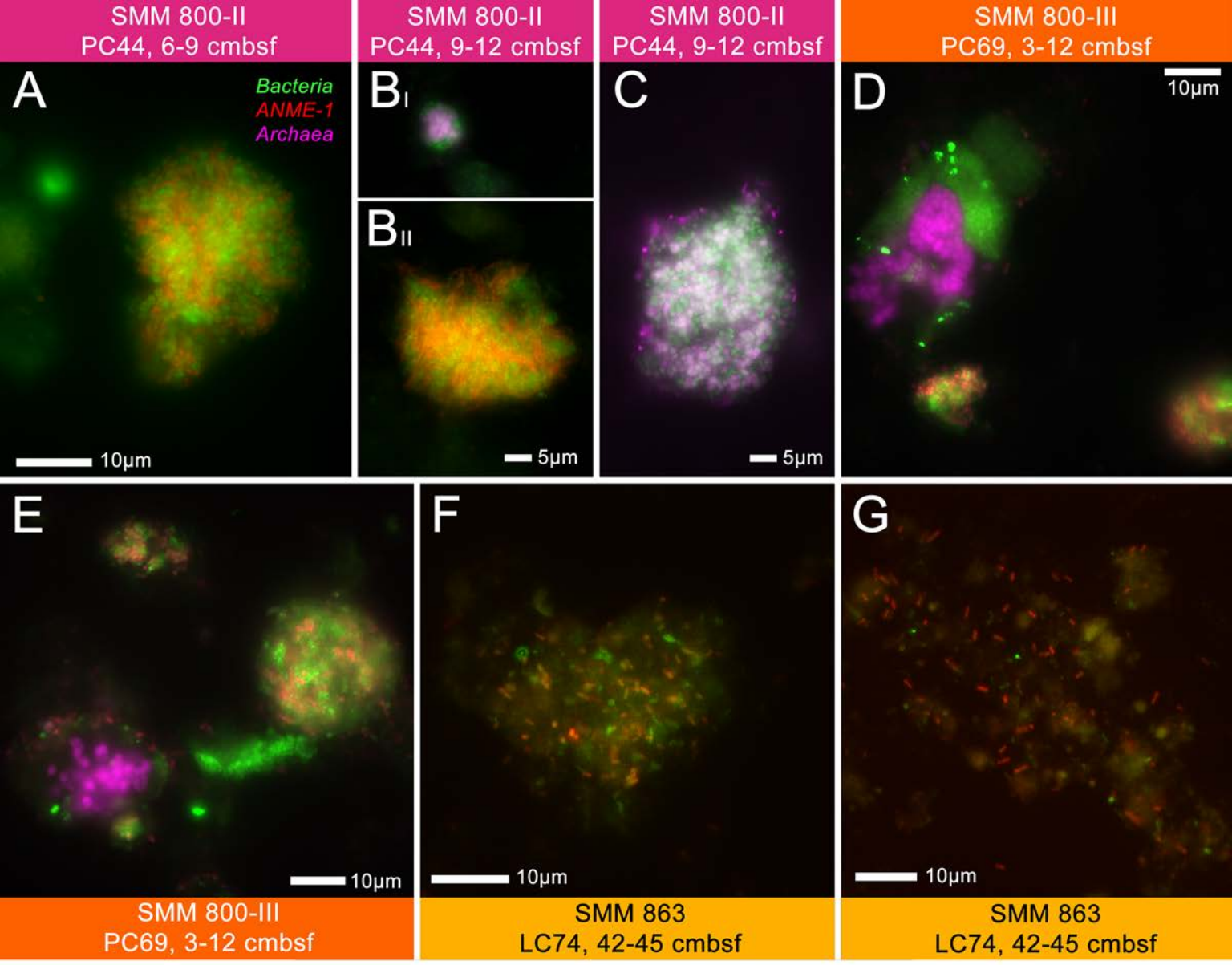


**Fig. 9** – Representative examples of carbonate nodule associated cells and aggregates recovered from SMM 800-II, 800-III, and 863, visualized by fluorescence in situ hybridization (FISH) using probes targeting *Bacteria* (EUB338 I-III, in green), ANME-1 (ANME1-350, ANME1-728; in red), and *Archaea* (ARCH915, in pink). Cell extracts for nodules from SMM 800-I were not shown due to strong interference from auto-fluorescent exopolymeric material.

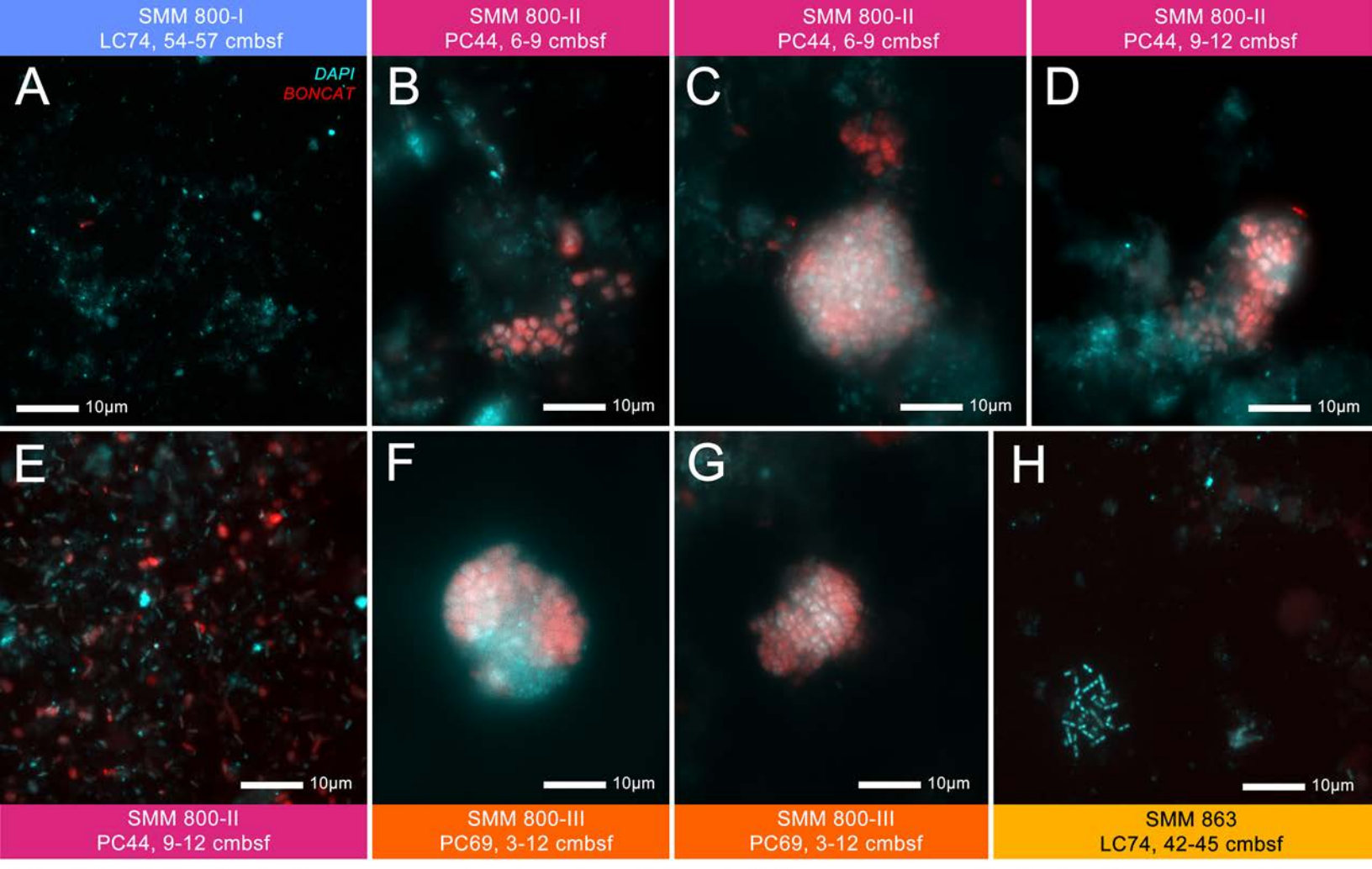


**Fig. 10** – Cell extracts from recovered carbonate nodules at all four seep areas, displaying the presence/absence of newly synthesized proteins with BONCAT (in red) after a 14-week incubation with methionine analog, L-Homopropargylglycine (HPG). DAPI staining of nucleic acids indicating cells is in cyan. Positive BONCAT signal was consistently observed in all extracts from the shallower nodules at SMM 800-II and 800-III, compared to the consistent lack of signal at SMM 800-I and 863.